RSC Advances

REVIEW

View Article Online
View Journal | View Issue

Cite this: *RSC Adv.*, 2020, **10**, 21427

Catalytic conversion of ethane to valuable products through non-oxidative dehydrogenation and dehydroaromatization

Hikaru Saito *[ab] and Yasushi Sekine [b]

Chemical utilization of ethane to produce valuable chemicals has become especially attractive since the expanded utilization of shale gas in the United States and associated petroleum gas in the Middle East. Catalytic conversion to ethylene and aromatic hydrocarbons through non-oxidative dehydrogenation and dehydroaromatization of ethane (EDH and EDA) are potentially beneficial technologies because of their high selectivity to products. The former represents an attractive alternative to conventional thermal cracking of ethane. The latter can produce valuable aromatic hydrocarbons from a cheap feedstock. Nevertheless, further progress in catalytic science and technology is indispensable to implement these processes beneficially. This review summarizes progress that has been achieved with non-oxidative EDH and EDA in terms of the nature of active sites and reaction mechanisms. Briefly, platinum-, chromium- and gallium-based catalysts have been introduced mainly for EDH, including effects of carbon dioxide co-feeding. Efforts to use EDA have emphasized zinc-modified MFI zeolite catalysts. Finally, some avenues for development of catalytic science and technology for ethane conversion are summarized.

Received 15th April 2020
Accepted 28th May 2020

DOI: 10.1039/d0ra03365k

rsc.li/rsc-advances

1. Introduction: chemical utilization of ethane

Chemical utilization of ethane (C_2H_6) has had great effects on the modern petroleum industry. Inexpensive ethane derived from shale gas and associated petroleum gases is widely available, respectively, in North America and in the Middle East.[1] Ethane is converted to ethylene (C_2H_4) by steam cracking without a catalyst in an ethane cracker. Ethylene is the most fundamental chemicals in petrochemical industry: 149.7 million tons of ethylene were produced in 2017 worldwide[2] to synthesize polyethylene, ethylene oxide, styrene, and other ethylene derivatives.

Ethylene production from ethane is far superior in terms of cost to production from naphtha, which is a conventional feedstock for ethylene production by the steam cracking. According to the literature,[1] costs of ethane were €46.28 and €145.96 per ton in Saudi Arabia and the United States,

[a]*Department of Materials Molecular Science, Institute for Molecular Science, 38 Nishigo-Naka, Myodaiji, Okazaki, Aichi 444-8585, Japan. E-mail: hsaito@ims.ac.jp; hikaru.3110.saito@gmail.com; Tel: +81 564 55 7287*

[b]*Department of Applied Chemistry, Waseda University, 3-4-1 Okubo, Shinjuku, Tokyo 169-8555, Japan*

Hikaru Saito received his PhD at Waseda University in 2020 under the supervision of Prof. Yasushi Sekine. His doctoral thesis focuses on catalytic conversion of ethane to ethylene and aromatic hydrocarbons. Since April 2020, he has worked as a JSPS research fellow at Institute for Molecular Science in the group of Assoc. Prof. Toshiki Sugimoto. His current research focuses on photo-catalytic conversion of methane.

Yasushi Sekine received his PhD from The University of Tokyo, 1998. He was appointed as an Assistant Professor of Department of Chemistry of The University of Tokyo in 1998, Waseda University in 2001, and was promoted to Associate Professor in 2007 and to Professor in 2012. His research interests are in the areas of catalysts, hydrogen production, methane/ethane activation, and catalysis in electric fields.

respectively, while those of naphtha were €708.56 and €669.58 per ton. As shown in Fig. 1, the global demand for ethylene will be expanded to 182.5 million tons in 2023 worldwide[2] due to the global increase in population and economic growth. Consequently, the feedstock for ethylene production will be shifted much from naphtha to ethane.

However, ethane cracking is an energy-intensive process because it necessitates high reaction temperatures (>1073 K). Therefore, ethylene production is favorably conducted at low temperatures to lower the energy consumption and carbon dioxide (CO_2) emission. Furthermore, development of ethylene production from ethane instead of naphtha has led to another difficulty. In addition to ethylene, fundamental chemicals including propylene, 1,3-butadiene, and aromatic hydrocarbons are produced by the steam cracking of naphtha. In contrast, these important building blocks are not obtained when using the ethane cracker.[1] Therefore, other methods to produce fundamental chemicals aside from ethylene must be used. For instance, propylene must then be produced through dehydrogenation of propane,[3] methanol to propylene,[4,5] or olefin metathesis of ethylene and 2-butenes.[6]

Catalytic conversion of ethane to ethylene and aromatic hydrocarbons is anticipated as key technologies to address those needs. Non-oxidative catalytic ethane dehydrogenation (EDH) over oxide or supported-metal catalysts has been investigated widely to achieve environmentally friendly ethylene production. As is the case in propylene production, aromatics including benzene, toluene, and xylenes (BTX), must be produced from feedstocks other than naphtha. BTX are important chemicals used for plastics production and pharmaceuticals synthesis. The global demand for BTX will increase from 111.2 million tons (BTX total) in 2017 to 141.0 million tons in 2023 worldwide (Fig. 1).[2] Catalytic ethane dehydroaromatization (EDA) is an attractive alternative to steam cracking of naphtha because valuable aromatics are produced from inexpensive ethane. In addition, EDA can be performed at relatively low temperatures with high BTX selectivity. Therefore, EDA is a potentially promising process for efficient BTX production from natural gas resources. Catalytic EDH and EDA under non-oxidative conditions are summarized in this review because some reviews of oxidative EDH have been published earlier.[7,8] Initially, steam cracking of ethane is introduced briefly based on its reaction mechanism. Next, details of non-oxidative EDH and EDA are described. Finally, perspectives for catalytic ethane conversion are discussed.

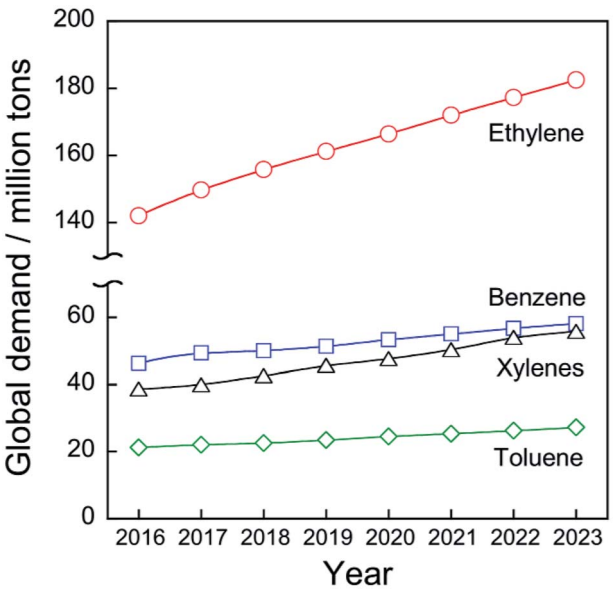

Fig. 1 History and projection of global demand for ethylene, benzene, toluene, and xylenes. Data originated from ref. 2.

2. Steam cracking of ethane

2.1. Radical chain reaction mechanism

Steam cracking of ethane is a non-catalytic process for ethane conversion to ethylene through pyrolysis. Before pyrolysis, ethane is mixed with effluent steam to supply reaction heat and to suppress carbonaceous deposits on cracking coils, where the reaction proceeds at *ca.* 1073 K. Ethane pyrolysis proceeds through a radical chain mechanism first proposed by Rice and Herzfeld.[9] This mechanism comprises various elementary reactions such as homolysis, hydrogen abstraction, hydrogen transfer, and recombination.[10] The reaction is initiated by homolytic cleavage of the C–C bond in an ethane molecule because enthalpy and the activation energy for the C–C bond dissociation is lower than that of the C–H bond dissociation.[11–14] The C–C bond cleavage in an ethane molecule leads to the formation of two methyl radicals as shown below.

$$C_2H_6 \rightarrow 2\cdot CH_3 \quad (1)$$

The methyl radical induces the subsequent propagation steps.

$$\cdot CH_3 + C_2H_6 \rightarrow CH_4 + \cdot C_2H_5 \quad (2)$$

$$\cdot C_2H_5 + \cdot CH_3 \rightarrow C_2H_4 + CH_4 \quad (3)$$

$$\cdot CH_3 + C_2H_6 \rightarrow \cdot C_3H_9 \quad (4)$$

$$\cdot CH_3 + C_2H_4 \rightarrow \cdot C_3H_7 \quad (5)$$

$$\cdot C_3H_9 + \cdot CH_3 \rightarrow C_3H_8 + CH_4 \quad (6)$$

$$\cdot C_3H_7 + \cdot CH_3 \rightarrow C_3H_6 + CH_4 \quad (7)$$

A hydrogen atom in an ethane molecule is first abstracted by the methyl radical, resulting in the formation of a methane and an ethyl radical (reaction (2)). Subsequent hydrogen transfer in the ethyl radical engenders the formation of ethylene and methane molecules (reaction (3)). The methyl radical also attacks ethane and ethylene (reactions (4) and (5)), resulting in the formation of propane and propylene (reactions (6) and (7)). Heavy hydrocarbons are obtainable through analogous reactions. Furthermore, termination steps proceed through reactions between two radicals.

$$\cdot CH_3 + \cdot CH_3 \rightarrow C_2H_6 \quad (8)$$

Based on the temperature programmed reaction, pyrolysis of ethane to ethylene initiates at higher than 873 K.[15] Under a practical situation, many reactions proceed in addition to the reactions (1)–(8). Sundaram and Froment considered 49 reactions to simulate the product distribution and concentration of radicals.[13] The cracking coil is a tubular reactor. Therefore, the temperature gradient along the radial direction is an important factor to be incorporated into calculation of the product distribution and concentration of the radicals. Marin and co-workers reported that the methyl radical concentration is higher near the cracking coil wall than at its center because of high temperatures near the wall, which are the result of endothermicity.[14] This phenomenon results in methane formation in great quantities if the simulation is based on a two-dimensional model.

Formation of by-products such as methane, C_3, and heavier hydrocarbons is unavoidable in the case of ethylene production through the radical chain mechanism because the reaction initiates from the C–C bond cleavage; it also terminates with methane formation. Particularly, the formation of methane and coke, which are thermodynamically stable, is remarkable at high conversion (temperature) levels.[16,17] This remarkable formation decreases the efficiency for ethylene production.

2.2. Coke formation and its suppression

Coke formation on the internal wall of the cracking coils induces severe difficulties such as a pressure drop and a decrease in heat flux to the reactor.[18] The latter particularly decreases the ethylene yield because of a kinetic restriction by decreased temperature. To maintain high ethylene yields, the outlet gas temperature is generally operated as constant, which indicates that the cracking coil is heated much more than usual to supply sufficient heat flux, thereby creating a higher temperature of the internal wall than the reaction temperature. Therefore, taking the thermal resistance of the cracking coil and the tolerable pressure drop into consideration, periodic removal of the carbonaceous deposits (decoking) is conducted every 20–60 days depending on operational conditions.[17,19] In general, coke formation mechanisms of three types have been proposed: the heterogeneous catalytic mechanism, the heterogeneous radical mechanism, and the homogeneous condensation mechanism.[20] The heterogeneous catalytic mechanism is based on coke formation on the surface of the cracking coils. The iron (Fe) and nickel (Ni) included in iron–chromium–nickel (Fe–Cr–Ni) alloys, which are used as cracking coil materials, catalytically promote coke formation on their surface. This phenomenon is observed at the initial stage of the reaction until the cracking coil surface is covered with carbonaceous deposits, indicating that the coke formation rate decreases gradually and reaches an asymptotic value.[17,21] The heterogeneous radical mechanism is based on the growth of the carbonaceous deposits through reactions with the radical species. Wauters and Marin proposed that this mechanism comprises five steps: hydrogen abstraction, substitution, addition by radicals, addition to olefins, and cyclization.[22] Once the coke forms on the wall, the growth of coke proceeds throughout the reaction. The carbonaceous deposits can also be formed through the homogeneous condensation mechanism as a result of the chain reaction. Therefore, the coke formation *via* this route is concomitant with the pyrolysis of ethane.

From a metallurgic perspective, coating the surface with inert oxides is an effective means of mitigating the coke formation. In principle, aluminum (Al) or manganese (Mn) is included in the Fe–Cr–Ni alloys. After oxidation of the alloy at high temperatures (1323 K for Al; 1023 K for Mn), alumina (Al_2O_3) or manganese chromate ($MnCr_2O_4$), which has high coking suppression capability, is deposited on the surface.[20,23] Recently, coating a catalyst for the water gas reaction has been developed to achieve operations without coke formation.

$$\mathrm{C(s,\ graphite) + H_2O(g) \rightarrow CO(g) + H_2(g)},\ \Delta_r H^\theta\ (298\ \mathrm{K}) = 131\ \mathrm{kJ\ mol^{-1}} \quad (9)$$

For instance, BASF developed the CAMOL® process to mitigate coke formation. In this case, tungsten-containing oxides are used as catalysts.[24] General Electric also developed gasification catalysts that include perovskite oxides containing cerium (Ce) and alkaline-earth metals.[25] However, introduction of the catalysts to cracking coils remains an immature technology. Further research and development are necessary in the domain of catalytic science.

3. Dehydrogenation of ethane under non-oxidative conditions

Catalytic ethane dehydrogenation, denoted as EDH, enables ethylene production at lower temperatures than those of pyrolysis of ethane.

$$\mathrm{C_2H_6(g) \rightarrow C_2H_4(g) + H_2(g)},\ \Delta_r H^\theta\ (298\ \mathrm{K}) = 137\ \mathrm{kJ\ mol^{-1}} \quad (10)$$

However, the reaction is endothermic. Therefore, high reaction temperatures must achieve higher equilibrium conversion, as portrayed in Fig. 2. Furthermore, low pressure of ethane results in high equilibrium conversion based on Le Chaterlier's principle.

The EDH reaction mechanism is intrinsically unlike pyrolysis of ethane: catalysts should have ability of selective C–H bond dissociation. Side reactions such as hydrogenolysis of ethane and decomposition of ethane and ethylene to coke must be prohibited to achieve high and stable selectivity to ethylene. In this chapter, representative catalysts for EDH are described in terms of their active sites and reaction mechanisms.

3.1. Platinum-based catalysts

For dehydrogenation of alkanes (ethane, propane and butanes), platinum (Pt)-based catalysts have been used widely: one example is known as the Oleflex process.[26] In this process, the dehydrogenation reaction are performed by multiple fluidized bed reactors. The spent catalysts are continuously regenerated after the reaction. The regeneration processes are composed of removing carbonaceous deposits and re-dispersion of the Pt

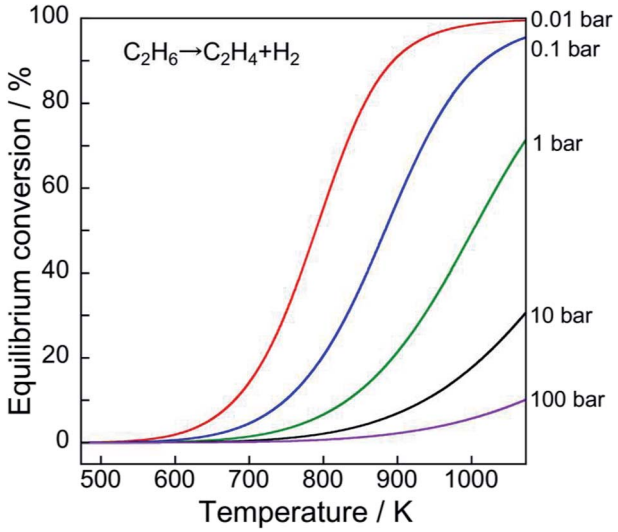

Fig. 2 Temperature dependence of equilibrium conversion of EDH at various ethane pressures.

particles with chlorine treatment.[27] The regenerated catalysts are, then, reused for the reaction. Since dehydrogenation reactions are endothermic, the Pt catalysts are used at high temperatures, which accelerate catalyst deactivations because of coke formation and agglomeration. Therefore, supported-Pt catalysts are modified with promoters such as tin (Sn) for improving their catalytic performance. In this section, we first introduce overview of supported-Pt catalysts. Subsequently, effects of the promoters on the nature of active sites are described in detail.

3.1.1. Overview of supported-platinum catalysts. A typical catalyst used for EDH is Pt/Al_2O_3. Highly dispersed Pt particles can exist on γ-Al_2O_3 by virtue of the presence of penta-coordinated Al, which stabilizes the Pt particles.[28,29] Calcined layered double hydroxides (hydrotalcite) are alternative candidates for use as a support material.[30–32] Particularly, Mg(Al)O hydrotalcite includes Al in its structure. The surface basicity can be expected to contribute to the suppression of coke formation, which results in deactivation of the catalyst. For dehydrogenation of propane, Pt/Mg(Al)O showed better performance than conventional alumina-supported catalysts, but coke formation is unavoidable.[33]

Surface active sites of two types are known to exist for Pt nanoparticles: coordinatively saturated Pt located at terrace sites and coordinatively unsaturated Pt (cus-Pt) such as step and edge sites. Both Pt sites are active for the C–H bond cleavage. However, the latter sites easily induce side reactions such as hydrogenolysis of ethane[34,35] and subsequent dehydrogenation of ethylene to coke[36,37] as shown in Fig. 3. However, Wu *et al.* calculated the turnover frequency (TOF) of ethane consumption using Pt/Mg(Al)O with different Pt particle sizes.[38] The TOF increased concomitantly with increased Pt particle size, whereas selectivity to ethylene was nearly constant, indicating that EDH proceeds at the terrace sites. This trend is not the case for propane dehydrogenation, where TOF decreases concomitantly with increased Pt particle size.[39]

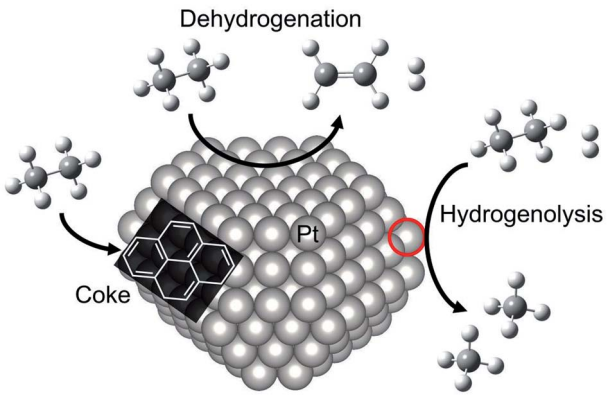

Fig. 3 Schematic image of reactivity of ethane on Pt particle. EDH proceeds on the Pt terrace sites, whereas coke formation and hydrogenolysis of ethane proceed on the "cus-Pt" sites circled in red.

The supported-Pt catalysts deactivate in two ways: coke formation and sintering (agglomeration). The carbonaceous deposits formed during the reaction cover the Pt surface and inhibit the access of reactants to active sites. To remove the carbon deposit, the spent catalysts are regenerated under oxidative atmospheres. In addition, the sintering of the Pt nanoparticles decreases the Pt surface area and the number of active sites. In contrast with dehydrogenation of propane and butanes, EDH necessitates the use of high reaction temperatures (>873 K), at which sintering of the Pt nanoparticles is accelerated. Consequently, Pt catalysts are exposed to severe environments: reductive (dehydrogenation) and oxidative (regeneration) atmospheres at high temperatures.

Co-feeding hydrogen (H_2) with ethane in the reaction system can inhibit coke formation. Galvita *et al.* demonstrated that positive effects can be produced for co-feeding H_2 on catalytic stability, but selectivity to ethylene decreases because of methane formation through hydrogenolysis.[40] Based on density functional theory (DFT) calculations,[41–43] high hydrogen coverage on the Pt surface inhibits the formation of coke precursors such as ethylidyne (CH_3C) and methylidyne (CH) species. In addition to suppression of the coke precursors, H_2 addition to the reaction system promotes ethylene formation under the kinetic conditions.[40] Hansen *et al.* applied DFT calculations to find that H_2 addition stabilizes the adsorbed ethylene and ethyl groups, leading not only to suppression of the coke precursors but to the facilitation of ethylene formation.[43]

Their practical use requires realization of the highly stable and dispersed Pt nanoparticles with coke formation in small amounts. To overcome these shortcomings, Pt catalysts are modified with promoters including boron (B), Al, copper (Cu), zinc (Zn), gallium (Ga), indium (In), and Sn.[38,40,44–58] Based on theoretical studies, silicon (Si) and germanium (Ge) are also good candidates for use as promoters.[59,60] Irrespective of the elements, the promoter effects are fundamentally classifiable into two types: geometric and electronic. In the following subsection, we describe the respective effects on the catalytic performance. Details of preparation methods,

characterizations, and other applications of Pt alloy catalysts are reviewed elsewhere.[61,62]

3.1.2. Geometric effects of promoters on platinum. Addition of the promoters to the supported Pt catalysts strongly influences the Pt active site structures. Geometric effects of various kinds are reported, such as surface modification, alloy formation, and re-dispersion. Among the promoters, we mainly describe Pt–Sn bimetallic catalysts because the traditional dehydrogenation catalysts are investigated thoroughly in detail.

The major role of the promoter is alloy formation. Addition of the promoters induces formation of Pt-based alloys or intermetallic compounds, as shown in Fig. 4(a). In addition to Sn,[38,40,56–58] other post-transition metals such as Zn, Ga, and In are used as promoters.[46–53] Fundamentally, Pt-based alloys are prepared by addition of the promoter and by subsequent reductive treatment. For Mg(Al)O support, some fraction of the Al can be replaced with Ga or In.[46,48,49,52] During the pre-reduction step, the dopants move from the partially reduced support to Pt, resulting in Pt-based alloy formation.

Catalytic performance, particularly selectivity to ethylene and stability, is enhanced by virtue of alloy formation. Alloy formation not only decreases the number of "cus-Pt" through replacement of "cus-Pt" atoms with the promoter: it also varies the surface composition (ensemble) of terrace Pt sites. Celik and co-workers used DFT calculations to elucidate coke formation from ethane on Pt(111) and Pt–Sn(111), representative terrace sites.[42] They constructed the alloy models by replacing the surface Pt atoms with Sn atoms, indicating that the model of PtSn has a face centered cubic (fcc) structure. They reported that CH_3C (coke precursor) is formed at three-fold Pt sites of Pt(111). For the PtSn(111) surface, where no three-fold Pt exists, CH_3C is unstable, leading to suppression of coke formation. They also predicted that a similar effect of alloy formation would be obtained using post-transition metals such as lead (Pb).[63]

In addition to the ensemble effect, alloy formation can alter the crystalline structure of Pt. Various Pt-based alloys form depending on the preparation conditions, including Pt/promoter ratios and pre-treatment conditions. For instance, Pt_3Sn and PtSn alloys can be prepared under different pre-treatment or reduction conditions, as investigated thoroughly by Deng *et al.*[64–67] For the dehydrogenation of ethane and propane, Pt_3Sn is suitable; it has the same crystalline structure (fcc) as that of metallic Pt,[38,65] whereas PtSn with a hexagonal close packing (hcp) structure is not active for propane.[65] The activity of PtSn for EDH has not been evaluated clearly yet. This is also the case in Pt–In catalysts, where Pt_3In exhibits higher activity than $PtIn_2$ (a fluorite structure).[53] Based on several studies, it seems plausible that the crystalline structure is an important factor for EDH. However, PtZn with a tetragonal gold–copper alloy (AuCu) structure is highly active for EDH.[51] Additional studies must be undertaken to elucidate the influence of the crystalline structure on EDH activity.

Surface modification is a geometric effect, as shown in Fig. 4(b). As described in Subsection 3.1.1, side reactions such as coke formation and hydrogenolysis are facile at the "cus-Pt" sites. These active sites can be covered by Sn addition if Pt–Sn alloys are formed or not, leading to suppression of the side reactions.[64] Similar effects of Al addition were also reported by Peng *et al.*[37] The surface Sn species, which do not contribute to Pt–Sn alloy, exist on "cus-Pt" as Sn oxides such as SnO_2. The location of Sn is evaluated using infrared (IR) spectroscopy with carbon monoxide (CO) as a probe molecule.[55,64,67,68] Broad absorption bands for linearly adsorbed CO and weak absorption bands for bridged CO on monometallic Pt are observable, respectively, at around 2080 and 1850 cm^{-1}.[55,64] In this case, CO linearly adsorbed onto "cus-Pt" shows the absorption bands at slightly lower wavenumbers than that on Pt terrace because "cus-Pt" interacts strongly with CO, resulting in much back donation from Pt to $2\pi^*$ (anti-bonding) orbitals of CO. Deng *et al.* reported that absorption bands attributed to CO_2 are observed in the spectrum of Pt modified with SnO_2.[64] However, no CO_2 formation was verified without SnO_2. The Pt modified with SnO_2 exhibits higher selectivity for dehydrogenation of propane and butane. Therefore, they concluded that SnO_2 exists on the Pt surface, where it covers "cus-Pt". On Pt_3Sn and PtSn surfaces, linearly adsorbed CO shows symmetric absorption bands because of the few "cus-Pt" sites. Furthermore, the absorption bands for bridged CO were not apparent, even on Pt_3Sn. The existence of multi-coordinated CO was verified on well-defined $Pt_3Sn(111)$.[69] This difference is ascribed to the

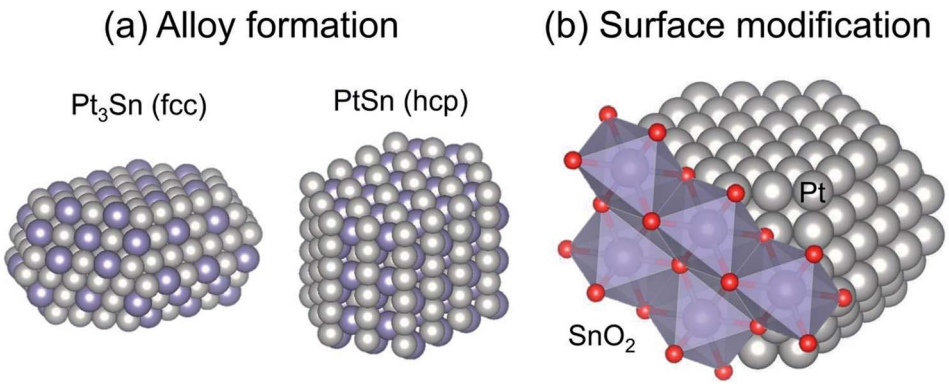

Fig. 4 Typical geometric effects of Sn addition to Pt: (a) alloy formation and (b) surface modification. Face centered cubic and hexagonal close packing are denoted respectively as fcc and hcp.

surface enrichment of Sn on Pt_3Sn and PtSn nanoparticles. Deng *et al.* applied X-ray photoelectron spectroscopy (XPS) and found that the surface Sn/Pt ratios are higher than those of bulk material,[66,67] indicating that surface modification of SnO_2 occurs concomitantly with alloy formation. It is worth noticing that segregation of Sn from Pt–Sn alloys[70,71] and surface reconstruction of metallic Pt nanoparticles[72] occur through CO adsorption. These phenomena alter the wavenumbers and shape of the CO absorption bands. Therefore, the information obtained from the IR spectra would not appropriately reflect the working state of the Pt and Pt–Sn surfaces.

The Pt particle size (dispersion) can be varied by promoter addition. For example, small Pt particles are obtained by Sn addition using silica supports.[64,73] Such is not the case for γ-Al_2O_3 and Mg(Al)O because these Al containing supports stabilize Pt particles,[28,29] leading to small Pt particles (<*ca.* 3 nm) even without Sn.[38,74] In addition, Sn plays a crucially important role in re-dispersion of the Pt particles through oxidative and subsequent reduction treatments for catalyst regeneration, as presented in Fig. 5. Weckhuysen and co-workers reported characteristic behavior of the re-dispersive effect of Sn on the Pt particles during regeneration based on CO adsorption, *in situ* X-ray absorption fine structure (XAFS) spectroscopy, and transmission electron microscopy.[74,75] They observed atomically dispersed Sn on γ-Al_2O_3, which plays a role in nucleation sites for re-dispersion of Pt (Fig. 5(a)). During the oxidative treatment, Sn segregates from the alloy; platinum oxide (PtO) is formed on the support (Fig. 5(b)).[76] Subsequent reductive treatment reconstructs the Pt–Sn alloy.[75] Therefore, they argued that the agglomeration of Pt is more responsible for deactivation than carbon deposition.[74] The phenomena occurring during oxidation are expected to be crucially important for the re-dispersion of Pt–Sn alloy. However, the nucleation mechanism and the role of segregated Sn have not been clearly proved.

3.1.3. Electronic effects of promoters on platinum. Modification of the electronic state of Pt is the other role of the promoters. Particularly, effects of Sn addition on the electronic state of Pt were examined mainly based on Pt L_{III}-edge XAFS spectroscopy.[64–67,76,77] The absorption edge energy of Sn-modified Pt catalysts is shifted to higher values than that of bare Pt catalysts. This finding apparently indicates electron-deficient Pt formation by Sn addition. However, the shift of the edge energy, which represents the transition energy of electrons from $2p_{3/2}$ orbital to vacant 5d orbital, is attributed to an increase in the energy level of the vacant 5d orbital. Therefore, the shift does not indicate the electronic density of Pt accurately. Deng *et al.* evaluated the electronic state of Pt by calculating d-band vacancy based on the white line intensity in Pt L_{III}-edge X-ray absorption near edge structure (XANES) spectra.[64] It is noteworthy that Pt catalysts with almost identical Pt particle size must be used for measurement because the metal particle size influences the white line intensity.[78–80] They argued that Pt with high electron density is obtained by Sn addition if Pt–Sn alloys composed mainly of Pt_3Sn are formed or not, indicating that even modification of Pt with SnO_2 induces electron donation from Sn to Pt, as shown in Fig. 6(a). Therefore, they conclude that Sn addition makes Pt electron-rich. The electron donation of Sn to Pt is also verified by DFT calculations.[42]

The electron donation from Sn to Pt can be supported by CO adsorption using IR spectroscopy. The absorption bands for CO linearly adsorbed onto Pt_3Sn or PtSn show at lower wavenumbers than that on monometallic Pt terrace.[64,67,68] The shift of the absorption bands is based on formation of electron-rich

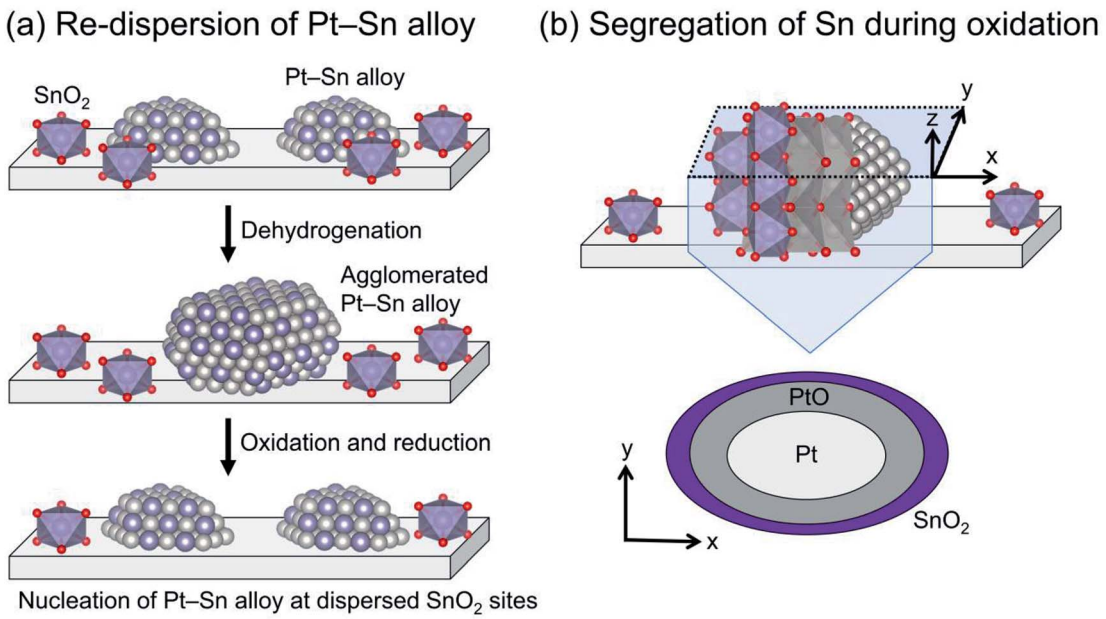

Fig. 5 Schematic images of (a) re-dispersion of Pt–Sn alloy through oxidation and subsequent reduction (regeneration) and (b) segregation of Sn from Pt–Sn alloy during oxidation.

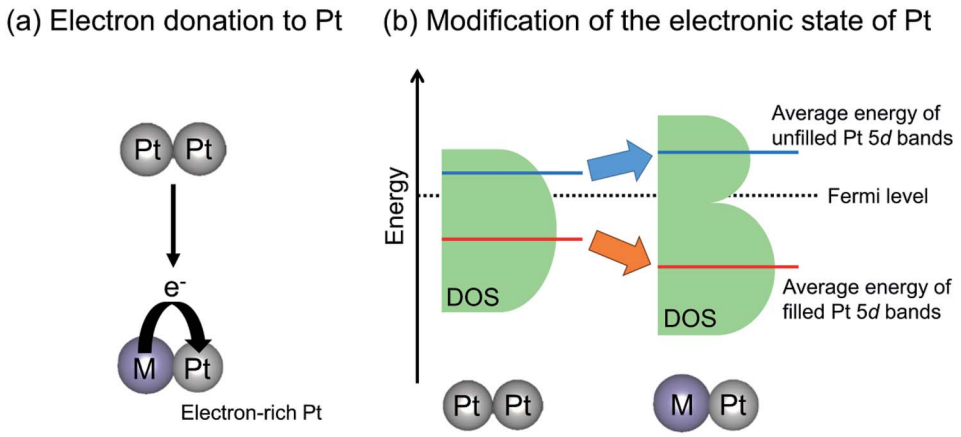

Fig. 6 Proposed effects of the promoters on the electronic state of Pt: (a) electron donation from the promoter (M) to Pt and (b) modification of the energy level of Pt 5d bands. Densities of states are denoted as DOS.

Pt by alloy formation, resulting in much back-donation from Pt to CO. However, the following two factors must be considered: (i) Pt–Sn alloy has no "cus-Pt" and (ii) the spectra for CO adsorption are measured under the same coverage of CO.[81] In the former case, the absorption band shape corresponding to CO adsorbed onto Pt–Sn alloy is sharp compared to that on monometallic Pt. Ideally, the bands should be symmetric to demonstrate that Pt–Sn has environmentally uniform active sites. The latter case is related to dipole–dipole interactions between CO and adjacent CO adsorbed at Pt sites. On the Pt–Sn alloy surface, the number of Pt sites for CO adsorption is diluted with Sn. This dilution induces low coverage of CO and weak dipole–dipole interactions, resulting in low wavenumbers of bands for linearly adsorbed CO.

In contrast with electron donation, Xin *et al.* argued that the electronic effects of Sn on Pt are not electron donation but the change in the energy level of d-band center of Pt through the hybridization of Pt 5d bands with Sn valence (5s and 5p) bands.[77,82] Recently, Miller and co-workers investigated the electronic structure of Pt in PtZn and Pt–Fe (Pt_3Fe, PtFe and $PtFe_3$) intermetallic compounds using resonant inelastic X-ray scattering to evaluate the energy level of Pt 5d orbitals.[51,83] They reported that the average energy gap separating the filled and unfilled Pt 5d bands is expanded compared with that of monometallic Pt. In other words, Zn or Fe addition stabilized the energy level of the occupied 5d band, whereas the unoccupied 5d band is shifted to higher energy levels, as shown in Fig. 6(b). Additionally, they calculated the projected d density of states localized on Pt atoms.[83] The mean energy of filled (below the Fermi level) Pt 5d bands is stabilized by virtue of alloy formation, whereas that of unfilled (above the Fermi level) Pt 5d bands is shifted upward. Therefore, they proposed that the alloy formation effect on the electronic state of Pt is the modification of the energy level of the Pt 5d bands rather than electron donation from the promoters to Pt. This change in the Pt 5d band energy is expected to affect the platinum–ethane interaction and to enhance the catalytic activity.

The change in the electronic state of Pt modified with the promoters influences the adsorption properties of intermediates and products. Hook *et al.* calculated the binding energy of the intermediates on Pt and Pt–Sn(111) surfaces based on DFT.[44] From their results, they reported that ethylene adsorbs weakly on the Pt–Sn surface, indicating that re-adsorption of ethylene, which induces ethylene decomposition to coke, can be inhibited on the surface. Such is also the case in the binding energy of the coke precursors. Generally, ethylene adsorbs on Pt in either π-bonded or di-σ-bonded configuration.[84] The latter adsorbs on the Pt surface more strongly, resulting in ethylene decomposition. Sn addition to Pt inhibits ethylene adsorption on Pt, as demonstrated by Liwu *et al.*[85] However, large amounts of carbon deposition were verified in the case of Pt–Sn/γ-Al_2O_3.[74,86] This phenomenon is based on the drain-off mechanism proposed by Lieske *et al.* and modified by Kumar *et al.*[73,86] As shown in Fig. 7, the coke precursors weakly adsorbed onto Pt–Sn are facile to transfer from the Pt–Sn surface to γ-Al_2O_3. Then, coke formation proceeds on the support. This coke is burnable at higher temperatures than that deposited on Pt.[85] In this way, Sn addition to Pt not only contributes to the suppression of coke formation; it also keeps the Pt–Sn surface clean.

3.2. Chromium-based catalysts

Chromium (Cr) oxide catalysts have been used for dehydrogenation of light alkanes, as represented by the Catofin process (Mcdermott-Lummus).[26] The dehydrogenation reactions are performed by multiple fixed bed reactors operated in the cyclic mode (reaction and regeneration).[87] During the operation, several reactors are used for the reactions while catalyst regeneration is conducted in the others. Among the products, hydrogen is separated by a pressure swing adsorption unit. The unreacted feed is separated from the products and recycled for the reactions. The Catofine process is employed for dehydrogenation of propane and butanes, similarly to the Oleflex process. In terms of cost, the Cr oxide catalysts is superior to Pt-based catalysts. As described in this section, thorough

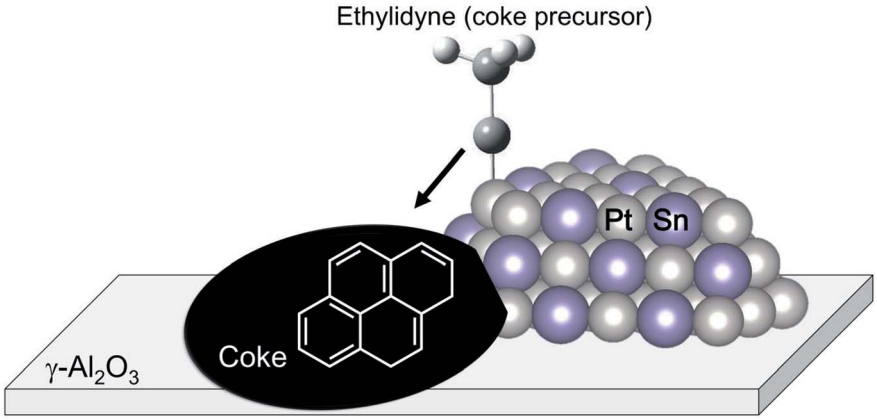

Fig. 7 Schematic image of the drain-off mechanism. Coke precursors such as ethylidyne move to the supports on which coke formation proceeds.

investigations have been conducted of the active sites, effects of support, and influences of co-feeding CO_2 in order to use the Cr oxide catalysts for EDH.

3.2.1. Active sites of chromium species for EDH. The nature of Cr species is an important factor affecting C–H bond activation. Fundamentally, EDH proceeds on Cr–O sites.[88] Their structures and electronic states have been investigated using various characterizations such as temperature-programmed reduction (TPR), Raman spectroscopy, ultra violet (UV)-visible (Vis) spectroscopy, X-ray diffraction, XAFS spectroscopy, and XPS.[89–96]

The Cr species can be various structures. Generally, the Cr species are classifiable into four types: monochromate (isolated mononuclear Cr), polychromate (Cr oxide cluster), amorphous Cr oxide (Cr_2O_3) and crystalline α-Cr_2O_3.[90–92,94] The Cr species structure is mainly dependent on the amount of Cr loading. At the high loading amount (>5 wt%), the amorphous Cr_2O_3 and crystalline α-Cr_2O_3 are easily formed. These Cr species are regarded as inactive for dehydrogenation.[90,97] In contrast, monochromate and polychromate species are dominant at low loading amount. The formation of Cr_2O_3 is distinguishable from the color of the catalysts: actually, the color is varied from yellowish to greenish because of the Cr_2O_3 formation.[95,98,99]

Investigations of the nature of monochromate and polychromate have been conducted widely because these Cr species are active sites for EDH.[87,100,101] Images of them are presented in Fig. 8. To identify the existence of the Cr species, UV-Vis and Raman spectroscopy are useful techniques. However, the Cr species are reduced under the reaction conditions from Cr^{6+} or Cr^{5+} to Cr^{3+} or Cr^{2+}. Therefore, evaluating the active sites under *in situ* conditions is important. For fresh Cr oxide catalysts, Cr^{6+} is dominant. Many studies have specifically examined Cr^{6+} because the existence of Cr^{5+} was identified only by electron spin resonance (ESR) and IR spectroscopy.[91,98] In addition, the reduced Cr species are mainly Cr^{3+}. Although Cr^{2+} was identified using XPS and XAFS,[96,100] the proportion of Cr^{2+} in the spent catalysts was rather small.[100] Therefore, Cr^{6+} is considered to be reduced to Cr^{3+} during the dehydrogenation reaction. The nature of Cr^{5+} and Cr^{2+} remains under discussion.

The EDH over Cr oxide catalysts proceeds on the reduced monochromate and polychromate. As presented in Fig. 9(a), Olsbey *et al.* reported based on results of an isotopic study that end-on and dissociative adsorption of ethane occurs on the active sites.[88] However, Shee and Sayari observed adsorbed acetaldehyde using diffuse reflectance infrared Fourier transform (DRIFT) spectroscopy.[102] They proposed that the ethoxide species formation is the first step in the dehydrogenation reaction (Fig. 9(b)). Determination of the adsorbed species on the respective Cr species is a challenging subject. Therefore, additional investigations based on, for instance, DFT calculations are expected to elucidate the reaction mechanism.

3.2.2. Effects of supports on the chromium state. As described in the preceding subsection, the ideal Cr oxide catalyst has as large an amount of monochromate or polychromate

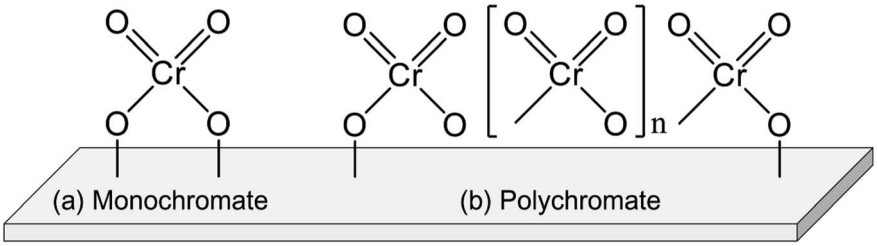

Fig. 8 Structure of (a) monochromate and (b) polychromate supported on a metal oxide.

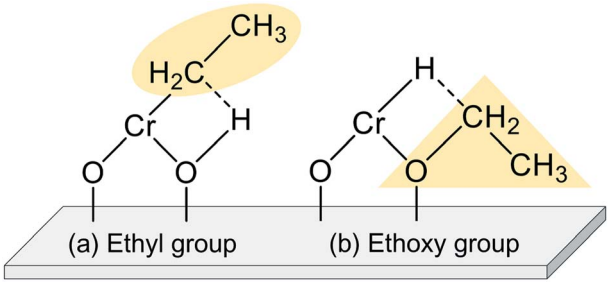

Fig. 9 Schematic adsorption of ethane on reduced monochromate supported on a metal oxide: formation of (a) ethyl group and (b) ethoxy group.

species as possible. However, the large Cr loading amount results in the formation of the inactive Cr_2O_3 species through agglomeration.[95] Therefore, selection of an appropriate support strongly influences the catalytic activity and ethylene selectivity.

Alumina is a typical support for this purpose.[88–92,95,102] Recently, Fridman *et al.* thoroughly examined the Cr species on the alumina support.[95] They reported that a part of the monochromate and polychromate was unstable and reduced during dehydrogenation of isobutane. After the reduction, small Cr_2O_3 clusters were agglomerated; large Cr_2O_3 clusters were formed. Furthermore, regeneration of the catalyst under oxidative conditions induced formation of aluminum–chromium–chromate species around the periphery of the Cr_2O_3 clusters, as shown in Fig. 10. Agglomeration of the monochromate and polychromate leads to irreversible deactivation of the catalysts.

Silica (SiO_2) is an alternative support to alumina. Silica support of various kinds, including silicious-zeolites and mesoporous silica, were examined.[94–100,103–106] These silica supports have a large surface area, resulting in highly dispersed Cr species on the supports. The amount of silanol (SiOH) groups is expected to play an important role in stabilizing the dispersed Cr species (monochromate or polychromate). Cheng *et al.* reported that the initial activity of Cr/SBA-15 (mesoporous silica) is proportional to the amount of the SiOH groups contributing to the abundantly dispersed Cr species.[105] Botavina *et al.* proposed detailed structures of monochromate based on XAFS measurements.[96] The reduced monochromate was bound with two short Si–O–Cr bonds and a long Si–O–Cr bond. Its electronic state is expected to be Cr^{2+} rather than Cr^{3+}. These studies indicate that the density of the SiOH groups influences the Cr active site characteristics.

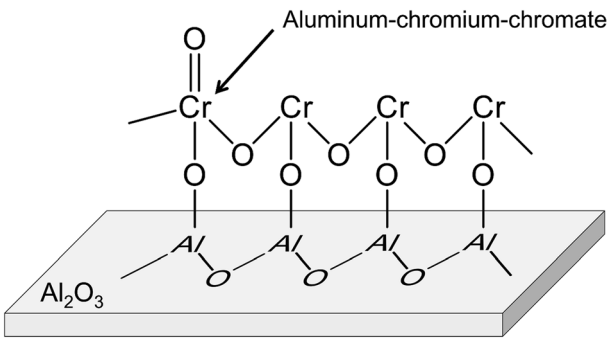

Fig. 10 Structure of aluminum–chromium–chromate.

3.2.3. Co-feed of carbon dioxide in EDH over chromium-based catalysts. To enhance the catalytic performance of the Cr catalysts, EDH has been investigated in the presence of CO_2.[107] In many cases, EDH in the presence of CO_2 is regarded as oxidative dehydrogenation. However, the overall reaction is still endothermic, as presented below.

$$C_2H_6(g) + CO_2(g) \rightarrow C_2H_4(g) + CO(g) + H_2O(g),\ \Delta_r H^0\ (298\ K) = 178\ kJ\ mol^{-1} \quad (11)$$

This chemical formula is interpreted as EDH (reaction (10)) in combination with the reverse water gas shift (RWGS) reaction.

$$CO_2(g) + H_2(g) \rightarrow CO(g) + H_2O(g),\ \Delta_r H^0\ (298\ K) = 41.2\ kJ\ mol^{-1} \quad (12)$$

Therefore, the reaction (11) characteristics differ completely from those of oxidative EDH using oxygen as an oxidizing agent, which is an exothermic reaction. Effects of the CO_2 introduction to the dehydrogenation system are generally explained based on the following three reasons:[108–110] decrease in the partial pressure of ethane (see also Fig. 2); removal of H_2 from the reaction system through RWGS, resulting in the promotion of EDH; and improvement of catalytic stability by virtue of removal of carbonaceous deposits through the reverse Boudart reaction.

$$C(s,\ graphite) + CO_2(g) \rightarrow 2CO(g),\ \Delta_r H^0\ (298\ K) = 172\ kJ\ mol^{-1} \quad (13)$$

The promotion of ethane conversion and suppression of coke formation have been reported.[99,109] However, the promotive effect on EDH over Cr-based catalysts is attributed not only to the contribution of RWGS but to differences in the nature of active sites and reaction mechanism. Without CO_2, the active sites are presumed to be Cr^{3+} reduced from monochromate or polychromate (Cr^{6+}). At the initial stage of the reaction, where the reduction of Cr^{6+} proceeds, ethane conversion tends to decrease,[100,101] indicating that Cr^{6+} is more active than Cr^{3+} for EDH. Indeed, Mimura *et al.* reported that the apparent activation energy of EDH decreased from 119.3 (without CO_2) to 91.3 (with CO_2) kJ mol^{-1} using a Cr/ZSM-5 (zeolite) catalyst.[98] Therefore, it is proposed that EDH proceeds through the redox mechanism as shown in Scheme 1. In this scheme, ethane is activated oxidatively at Cr^{6+}=O sites, resulting in the formation of ethylene and water (H_2O). Then, the catalytic cycle is completed through oxidation of the reduced Cr^{3+} species with CO_2. Among the Cr species, Baek *et al.* proposed based on TPR that the large amount of polychromate results in a high catalytic activity for dehydrogenation of propane in the presence of CO_2.[111] Therefore, polychromate is expected to be the active site for EDH *via* the redox mechanism.

The redox behavior of the Cr species was verified using various techniques such as TPR, XPS, and IR spectroscopy. Based on TPR and XPS, the reduced Cr^{3+} can be oxidized to Cr^{6+}

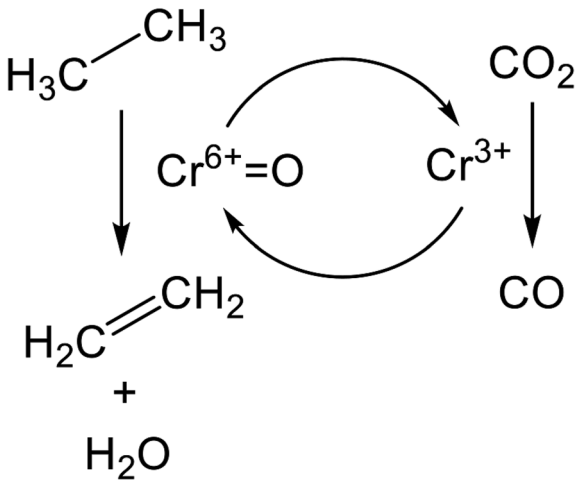

Scheme 1 Redox mechanism for EDH in the presence of CO_2 over Cr oxide catalysts.

under a CO_2 atmosphere.[99,104,109,110] In addition, Mimura *et al.* evaluated Cr=O bonds by IR spectroscopy,[98] demonstrating that the intensity of the absorption band attributed to Cr=O was decreased and increased respectively by ethane and CO_2 treatments. However, the reducible Cr^{6+} species are not re-oxidized completely with CO_2, probably because of agglomeration of monochromate and polychromate and because of the low oxidizing ability of CO_2.[112] Therefore, it is necessary for the catalyst to stabilize the reducible Cr^{6+} species and to promote oxidation of the reduced Cr^{3+}. The silica supports are expected to be useful to stabilize the Cr active sites because of the presence of SiOH groups as described above. Recently, Al-Awadi *et al.* reported that modification of Cr/MCM-41 (mesoporous silica) with titania (TiO_2) nanoparticles enhances the concentration of Cr^{6+}, leading to high activity for EDH with CO_2.[113] To promote the oxidation of the reduced Cr species, the use of additives with oxygen storage capacity is one option.[114,115] In addition, CO_2 activation can be expected to be a key factor because of its low reactivity. Zirconia (ZrO_2)-supported Cr catalysts exhibited a high activity for EDH in the presence of CO_2 because of the basicity of ZrO_2 which would contribute to CO_2 activation.[110,116] The Zr promoter also increases the amount of reducible Cr^{6+}.[117]

Some difficulties remain unresolved in the case of EDH in the presence of CO_2. For instance, the contribution of CO_2 to oxidation of the reduced Cr species and RWGS, is not discussed in detail. One must elucidate the role of respective Cr species in dehydrogenation through the redox mechanism and RWGS. In addition, *operando* analyses in combination with isotopic CO_2 should be performed to prove the redox mechanism.

3.3. Gallium-based catalysts

Several Ga oxide catalysts are known to have catalytic activity for EDH.[118] Actually, Ga catalysts are classified into two types: zeolite-supported Ga oxide catalysts and other metal oxide-supported Ga oxide catalysts. Comparison of zeolite supports with other metal oxide supports such as Al_2O_3 and TiO_2 reveals that characteristics of the active sites differ because of the cation-exchange ability of zeolite. In this regard, differences in the characteristics of the active sites, which are derived from properties of the supports, are described.

3.3.1. Gallium-based catalysts supported on zeolites. Zeolite-supported Ga oxide catalysts were used originally for conversion of propane or butane into aromatic hydrocarbons.[119] The Cyclar process developed by BP/UOP is a representative example.[120] Among the zeolites, MFI type zeolite in proton form (H-ZSM-5) is used widely as a support. The characteristics of the Ga species, which can be formed by virtue of the ion-exchange ability of zeolite, have been investigated based on practical experiments and DFT calculations.

From a practical perspective, Ga/H-ZSM-5 catalysts prepared using various methods such as physical mixing, impregnation, and chemical vapor deposition (CVD) are used to elucidate the characteristics of the Ga species.[121–123] The pristine Ga/H-ZSM-5 usually contains highly dispersed Ga oxide species in the micropore system. At this stage, the Ga species are exchanged only insufficiently with the protons. To promote the ion-exchange, the Ga/H-ZSM-5 catalyst must be reduced under a H_2 atmosphere. This phenomenon was verified using *in situ* IR spectroscopy. Intensity of the absorption band at *ca.* 3610 cm^{-1} derived from acidic hydroxy groups (Si–OH–Al) decreases under H_2 atmospheres.[121,124] Simultaneously, a new absorption band attributed to GaO–H appeared at *ca.* 3660 cm^{-1}, clearly indicating the ion-exchange of the reduced Ga species with the acidic protons. Furthermore, formation of Ga–H bonds, which is unstable at high temperatures such as 573 K, was observed at room temperature. Based on findings obtained using IR spectroscopy, Ga^+, GaO^+, and $[GaH_2]^+$ are candidates for active sites of the reduced Ga/H-ZSM-5.[124,125] In addition, Rane *et al.* evaluated the electronic state of Ga using *in situ* Ga K-edge XANES spectroscopy.[123] At high temperatures (>673 K) under a H_2 atmosphere, a new feature was observed in a lower energy region (10 371 eV), indicating the formation of Ga^+. Subsequent cooling to 373 K induces the increase of a feature at 10 377 eV with disappearance of the spectrum at the low energy feature, indicating the formation of $[GaH_2]^+$. However, Getsoian *et al.* reported that the absorption edge energy was dependent not only on the electronic state of Ga but also on the type of ligand.[126] For instance, the absorption energy can be shifted to the lower position through the formation of low-coordinated Ga^{3+} alkyl or hydride species. However, Schreiber *et al.* performed quantitative analyses to elucidate the Ga species.[127] They conducted H_2 pulse tests at 873 K and measured the amount of the consumed H_2 and formed H_2O. As a result, they concluded that Ga^+ was formed after reduction at 873 K.

The activity of respective Ga species was evaluated experimentally. Rane *et al.* performed dehydrogenation of propane after reduction or oxidation treatments.[123] After reduction treatment to form $[GaH_2]^+$, the activity increased gradually with time on stream. In contrast, the activity of the oxidized Ga/H-ZSM-5 containing GaO^+ decreased rapidly in 1 h. These activities were close to that of Ga^+ species. They concluded that $[GaH_2]^+$ and GaO^+ are unstable active sites during the dehydrogenation of propane. Furthermore, the intrinsic activities of

the Ga species are in the order of $GaO^+ > Ga^+ > [GaH_2]^+$ based on the initial activities. However, Ausavasukhi and Sooknoi conducted EDH in a pulse reactor.[122] They demonstrated that the activity was enhanced by the introduction of H_2, indicating higher activity of $[GaH_2]^+$ for EDH than that of either Ga^+ or GaO^+. Moreover, the activity of $[GaH_2]^+$ decreased with subsequent C_2H_6 pulses under He, whereas high activity was maintained under H_2, indicating the unstable characteristics of the $[GaH_2]^+$. Therefore, the Ga^+ species would be stable during dehydrogenation reactions, although the activities of the Ga species for dehydrogenation of light alkanes would depend on the reactants. Nascimento and co-workers proposed that the reaction mechanisms were varied because of the size and type (linear or branched) of alkanes based on DFT studies.[128,129] In addition, differences in the reactor systems (flow or pulse reactor) must be examined because the adsorbed species, which would influence the activity, exist in a steady state using the flow reactor.

The reaction mechanism of EDH on the Ga species was investigated mainly using DFT calculations. As portrayed in Scheme 2, three reaction mechanisms have been proposed by some research groups:[128–133] the alkyl mechanism, the carbenium mechanism, and the concerted mechanism. The differences are based on the mode of ethane activation.

The alkyl mechanism begins from formation of $Ga–C_2H_5$ by hydrogen abstraction. By contrast, the carbenium mechanism proceeds through formation of an ethoxy group concomitantly with that of Ga–H. In the concerted mechanism, two hydrogen atoms are abstracted simultaneously from an ethane molecule, leading to the formation of ethylene and hydrogen in one step. The activation of ethane at Ga^+, $[GaH]^{2+}$, and $[GaH_2]^+$ sites is investigated by DFT calculations using cluster models. The alkyl mechanism is facile at any site.[128–132] However, Mansoor *et al.* recently reported that the carbenium mechanism is preferable at the $[GaH]^{2+}$ site.[133] In addition, Schreiber *et al.* proposed that the proximity between the Ga and Brønsted acid sites promotes the dehydrogenation of propane.[127] Experimentally, Kazansky *et al.* observed the adsorbed ethane on the Ga^+ sites using DRIFT spectroscopy.[125,134] They demonstrated the formation of $Ga–C_2H_5$ concomitantly with that of Ga–H. After heating, the absorption band of Ga–H at 2057 cm^{-1} was shifted to 2040 cm^{-1}, which is attributed to H–Ga–H, with the appearance of olefinic C–H. Therefore, EDH at the Ga^+ sites can be expected to proceed as the following Scheme 3.

The dehydrogenation activity of the GaO^+ species was evaluated in the presence of steam because the GaO^+ species are reduced under the reaction conditions.[123] Hensen *et al.* performed dehydrogenation of propane over Ga/H-ZSM-5 in the presence of steam.[135] As a result, stable activity was achieved. At the mononuclear GaO^+ site, the high activation barrier for hydrogen recombination was calculated among the elementary steps, resulting in the formation of a H_2O molecule and the Ga^+ site.[131] Therefore, they proposed that multinuclear GaO clusters are the active sites for the dehydrogenation reaction.[135–138] The Ga cations included in the clusters are favorable for tetrahedral coordination.[135] The proposed EDH at Ga_2O_2 clusters, for instance, is shown in Scheme 4. The dehydrogenation reaction proceeds at a Ga–O Lewis acid–base pair. Hydrogen recombination is facile at the Ga oxide clusters, although the H_2O formation is still favorable. Strong Lewis basicity of the bridged oxygen stabilizes the adsorbed hydrogen, resulting in the inhibition of the hydrogen recombination.[138] Therefore, Lewis basicity should be moderate to facilitate hydrogen desorption.

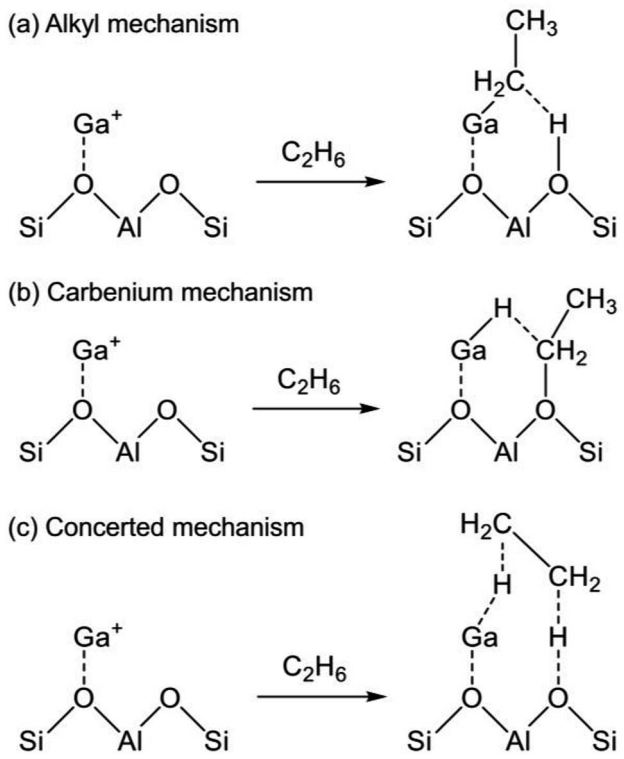

Scheme 2 Mechanism of ethane activation *via* (a) the alkyl mechanism, (b) the carbenium mechanism, and (c) the concerted mechanism. Ga^+ is a representative active site of Ga/H-ZSM-5.

3.3.2. Ga oxide (Ga_2O_3) catalysts. Supported Ga oxide catalysts such as Ga/TiO_2 are used for EDH, particularly, in the presence of CO_2.[139] On the supports, Ga oxide is fundamentally Ga_2O_3, which has five polymorphs (α-, β-, γ-, κ-, ε-Ga_2O_3).[140] Characterizations of Ga properties such as the structure of the active sites are indispensable because the surface Ga species play an important role in the reaction. Zheng *et al.* performed dehydrogenation of propane over Ga_2O_3 polymorphs, except for ε-Ga_2O_3.[141] As a result, β-Ga_2O_3, the most stable polymorph, exhibited the highest activity among them. They concluded that the tetrahedrally coordinated Ga^{3+} cations facilitate the dehydrogenation reaction. Recently, Seki *et al.* investigated the nature of active Ga species at the β-Ga_2O_3 surface for ethane activation.[142] Based on DFT calculations and on results of experimental measurements, ethylene strongly adsorbs on the surface tetrahedrally coordinated Ga species, probably resulting in ethylene decomposition to coke. In contrast, dissociative adsorption of ethane is favorable at the surface octahedrally coordinated Ga with coordinatively unsaturated, for instance, located at the β-Ga_2O_3(002) facet.

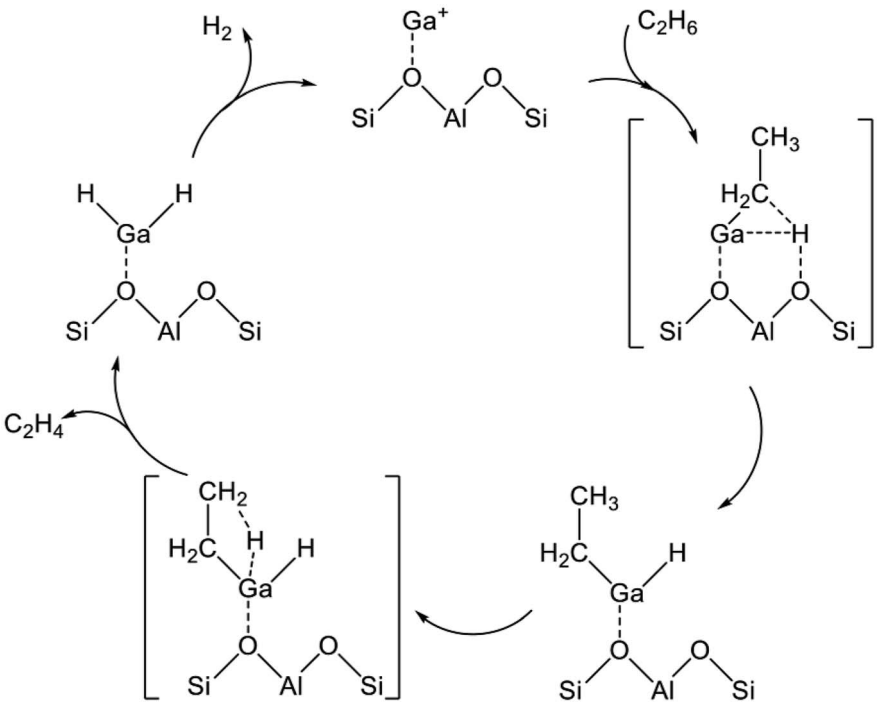

Scheme 3 Reaction mechanism of EDH at the Ga^+ site.

The coordination environment of Ga can be evaluated using Ga K-edge XANES. Nishi *et al.* conducted a quantitative analysis of tetrahedrally and octahedrally coordinated Ga using XANES spectroscopy.[143] Hereinafter, these Ga species are denoted respectively as Ga(T) and Ga(O). The analysis is based on deconvolution of the XANES spectra. It is applicable to Ga

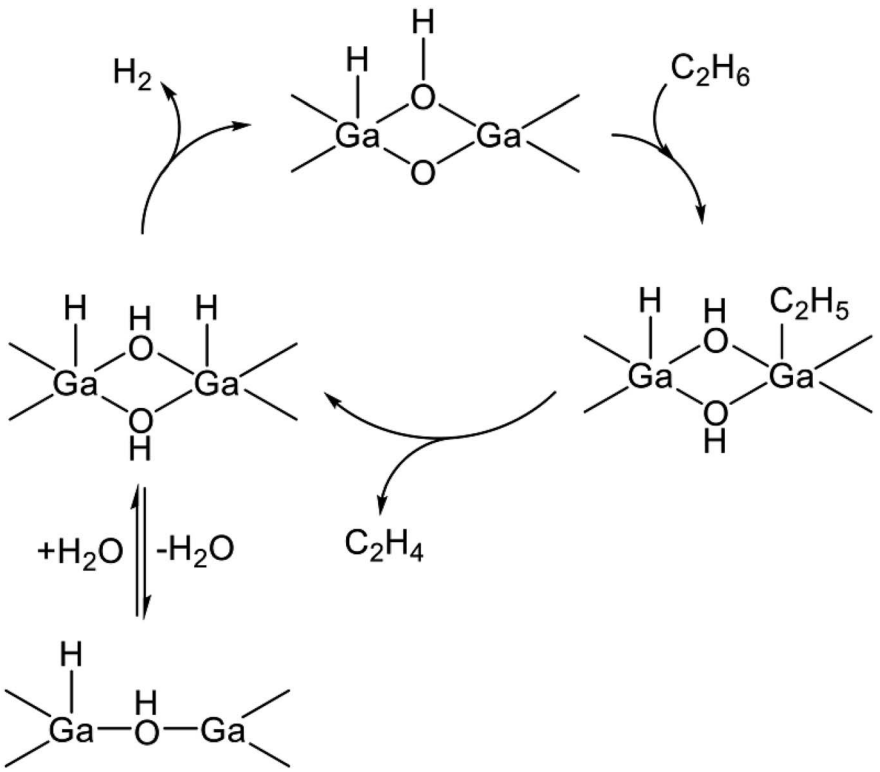

Scheme 4 Reaction mechanism of EDH in the presence of steam on a Ga oxide cluster.

polymorphs and supported Ga oxide catalysts.[143,144] In addition, the coordination environment of Ga_2O_3 can be evaluated by IR spectroscopy using H_2 as a molecular probe. Collins *et al.* reported that the absorption bands attributed to Ga–H bonds are observed at around 2000 cm^{-1}.[145] They further measured the spectra for hydrogen adsorbed onto α-, β-, and γ-Ga_2O_3.[146] The spectra consisted of absorption bands at 2003 and 1980 cm^{-1}. The contribution of the band at 1980 cm^{-1} was in the order of α-Ga_2O_3 > γ-Ga_2O_3 > β-Ga_2O_3. This order agrees with that of the fraction of Ga(O) in their structures. Therefore, they concluded that the Ga(T)–H and Ga(O)–H bonds are observed respectively at 2003 and 1980 cm^{-1}. The proportion of the surface Ga(T) to Ga(O) is calculable from the absorption band area. However, the band intensity is dependent on the temperatures.[147,148] At high temperatures such as 573 K, the intensity increased because of the formation of oxygen defects, resulting in the formation of new Ga–H bonds. Therefore, the coordination environment of surface Ga is expected to be evaluated appropriately at temperatures higher than 573 K because the dehydrogenation reaction is usually conducted at such higher temperatures under reductive conditions.

The reaction mechanism of EDH over Ga_2O_3 is similar to the alkyl mechanism over Ga/H-ZSM-5 (Scheme 3). Kazansky *et al.* measured the spectra for ethane adsorbed onto Ga_2O_3 using DRIFT spectroscopy.[149] In this case, the polymorph of Ga_2O_3 is not described clearly. They observed the formation of Ga–C_2H_5 in addition to C–H corresponding to CH_2 groups derived from ethylene, and Ga–H. The formation of Ga–C_2H_5 was also verified by ^{13}C cross-polarization magic angle spinning (MAS) nuclear magnetic resonance (NMR) spectroscopy.[150] In some cases, the formation of Ga–H and alkoxy groups was assumed to occur *via* the activation of light alkanes.[151,152] Nevertheless, no clear evidence of the formation of the alkoxy groups has been reported to date.

The dehydrogenation of ethane over Ga oxide catalysts is performed mainly in the presence of CO_2.[118] Nakagawa *et al.* reported that Ga/TiO_2 exhibited high activity when compared to other supports including Al_2O_3, SiO_2, ZrO_2, and zinc oxide (ZnO).[139] In the case of Ga/Al_2O_3, a negative effect on the catalytic activity was verified in the presence of CO_2. The promotive effects of CO_2 on EDH are attributed respectively to hydrogen and coke removal through the RWGS and the reverse Boudart reaction (reactions (12) and (13)).[153,154] In contrast, selectivity to ethylene tends to decrease with the increase in ethane activation.[155] Methane formation is promoted instead of the decrease in ethylene selectivity, indicating the subsequent conversion of ethylene to methane. Therefore, appropriate conditions such as space velocity and partial pressure of CO_2 are necessary to achieve high ethylene yield.

In contrast to Cr oxides, Ga_2O_3 is a non-reducible oxide. Therefore, no report has described the redox mechanism over Ga oxide catalysts in the presence of CO_2, although Ga species in H-ZSM-5 might have redox ability. To improve catalytic performance, designing Ga active sites is indispensable. For instance, Ga/H-ZSM-5 catalysts exhibited a higher selectivity to ethylene than β-Ga_2O_3.[156] Also, Ga/H-ZSM-5 exhibits the activity for RWGS, indicating that H_2O co-exists during EDH with CO_2. Therefore, the Ga oxide clusters, which exhibit high dehydrogenation activity *via* Scheme 4, would be maintained during the reaction.

3.4. Other catalysts and performance of EDH catalysts

Aside from Pt-, Cr- and Ga-based catalysts, cobalt (Co)- and molybdenum (Mo)-based catalysts exhibit catalytic activities for EDH.[157–163] Although Zn catalysts also have ethane activation ability,[134] they are applied for aromatization of light alkanes. Both are used mainly in the presence of CO_2. Among Co-based catalysts, the electronic state of Co is expected to be important. The existence of Co^{4+} promotes EDH *via* the redox mechanism similarly to the Cr catalysts.[157] However, Co^{2+} species facilitate RWGS analogously to the Ga catalysts.[158,159] For Mo-based catalysts, molybdenum carbide (Mo_2C) is rather more active for ethane activation than molybdenum oxide (MoO_3) in the presence of CO_2.[160] Chen and co-workers evaluated the electronic state of Mo using *in situ* XANES spectroscopy, revealing that Mo_2C is oxidized with CO_2.[161] They reported further that CO_2 is converted to CO and adsorbed oxygen over β-Mo_2C.[162] Therefore, the oxygen-modified Mo_2C (oxycarbide) would be formed and would promote EDH with CO_2.

Recently, lanthanum manganite ($LaMnO_3$) perovskites were applied for EDH. Yang *et al.* performed EDH without co-feed over reduced Ni-doped $LaMnO_3$.[164] They found that the proportion of Mn^{4+} increases and that Ni nanoparticles are deposited after reduction treatment with H_2. Therefore, they proposed that EDH proceeds on oxygen vacancies around Mn^{4+} and Ni nanoparticles. In contrast, Sekine and co-workers investigated EDH with H_2O over Ba-doped $LaMnO_3$.[165,166] They demonstrated clearly that EDH is promoted in the presence of steam because the reaction proceeds *via* the Mars–van Krevelen mechanism. They proposed that the amount of reducible Mn^{3+} is a key factor for ethylene formation. Ba doping enhances the redox properties of $LaMnO_3$ and the oxygens coordinated with Ba promote C–H activation of ethane.

Catalytic performance of the catalysts for EDH in the absence and presence of CO_2 is summarized respectively in Tables 1 and 2. In addition, ethylene selectivity *vs.* ethane conversion is shown in Fig. 11. The noble metal catalysts are used at low temperatures without CO_2, probably to suppress agglomeration and dry reforming. Yan *et al.* reported that modification of ceria (CeO_2)-supported Ni catalysts with Fe could mitigate dry reforming of ethane by virtue of iron oxide (FeO_x) located around periphery of Ni particles (Ni–CeO_2 interface).[167] Among the noble metals, palladium (Pd) and gold (Au) also exhibit the catalytic activity for EDH.[168,169] In order to replace the expensive noble metals, Ni_3Ga alloys,[170] which exhibited comparable catalytic performance of EDH to noble metal catalysts,[171] are good candidates. In recent studies, zeolite-supported metal catalysts appeared as new candidates for EDH without CO_2. The characteristic micropores and cation-exchange ability contribute to the formation of active sites such as highly dispersed iron carbides and indium hydrides.[172,173] In the presence of CO_2, Cr-based catalysts supported on various

Table 1 Catalytic performance for EDH in the absence of CO_2

No.	Catalyst	Temperature/K	C_2H_6 conversion/%	C_2H_4 selectivity/%	C_2H_4 yield/%	Ref.
1	PtSn/Mg(Al)O	873	2.6	100	2.6	40
2	Pt–In/SiO_2	873	15	99	15	53
3	PtSn–MgGaAlO	823	28	99	28	54
4	Pd–In/SiO_2	873	15	100	15	168
5	Au/SiO_2-doped TiO_2	923	16	95	15	169
6	Ni_3Ga/Al_2O_3	873	10	94	9.4	171
7	Cr/SBA-15/Al_2O_3/FeCrAl	1023	47	87	41	99
8	Cr/MCM-41	923	19	98	18	100
9	Cr–Ce/SBA-15	973	41	83	34	114
10	Cr_2O_3/Oxidized diamond	923	7.0	97	6.8	174
11	Cr/TS-1	923	52	86	45	175
12	Ga_2O_3/Al_2O_3	923	28	93	26	139
13	Ga/SiO_2-doped TiO_2	923	46	85	39	154
14	$La_{0.9}Mn_{0.8}Ni_{0.2}O_3$	1023	42	98	41	164
15	$La_{0.7}Ba_{0.3}MnO_{3-\delta}$	973	4.8	88	4.2	165
16	$Th_{0.75}Ca_{0.25}O_2$	998	48	78	37	177
17	Fe/ZSM-5	873	22	72	16	172
18	In–CHA	933	27	97	26	173

materials including oxidized diamond[174] and titanosilicate[175] exhibit high ethane conversion thanks to the redox mechanism (Scheme 1), which indicates that other materials with redox properties can be good catalysts. The metal oxides with redox properties are applicable to a chemical looping process.[176] Thorium (Th)- and Ni-based oxides are also reported to exhibit the activities[177,178] although comparative investigations are necessary to elucidate advantages of these materials.

3.5. Non-thermo-catalytic EDH

Recently, electrochemical and photocatalytic EDH was emerged as new approaches for ethylene production. These systems can be operated using renewable energy; ethylene can be produced by renewable electricity and sunlight. Therefore, electrochemical and photocatalytic EDH would play a crucial role in producing petrochemicals in a sustainable society.

3.5.1. Electrochemical EDH. Electrochemical EDH is performed by solid oxide electrolysis cells (SOEC) as shown in Fig. 12(a). Imposing electrochemical potential, oxidation/reduction reactions proceed on anode/cathode surfaces although SOEC must be heated to 673–973 K to obtain sufficient oxygen anion or proton conductivity.[179] At such temperatures, pyrolysis of ethane would be taken into account to calculate Faraday efficiency. Characteristically, pure hydrogen can be produced without separation

Table 2 Catalytic performance for EDH with CO_2

No.	Catalyst	Temperature/K	C_2H_6 conversion/%	C_2H_4 selectivity/%	C_2H_4 yield/%	CO_2/C_2H_6	Ref.
19	Cr/SBA-15/Al_2O_3/FeCrAl	1023	67	96	64	2	99
20	Cr_2O_3/SO_4–SiO_2	923	67	82	55	5	103
21	Cr/MSU-1	973	68	82	56	3	104
22	Cr/SBA-15	923	41	92	38	5	105
23	Cr/ZSM-5	923	66	75	49	5	106
24	Cr_2O_3/SiO_2	923	56	93	52	5	108
25	Cr/H-ZSM-5	923	68	70	47	9	109
26	Cr/Ti/MCM-41	973	52	93	48	5	113
27	Cr–Ce/SBA-15	973	55	96	53	3	114
28	Cr_2O_3/HZSM-5–ZrO_2	973	65	87	56	5	115
29	Fe–Cr/ZrO_2	923	54	93	50	3	116
30	Cr_2O_3/Oxidized diamond	923	27	87	24	5	174
31	Cr/TS-1	923	62	81	50	4	175
32	Ga_2O_3	923	29	87	25	5	139
33	Ga_2O_3/ZSM-5	923	25	92	23	5	151
34	Ga/SiO_2-doped TiO_2	923	47	78	37	5	154
35	Ga/TiO_2	973	38	57	22	2.5	155
36	Co–$BaCO_3$	923	48	92	44	3	157
37	CoO_x/SiO_2	973	46	85	39	2.5	159
38	Mo_2C	873	2.0	60	1.2	1	161
39	$Th_{0.75}Ca_{0.25}O_2$	998	46	97	45	0.78	177
40	CaO–NiO/Al_2O_3	973	28	56	16	0.75	178

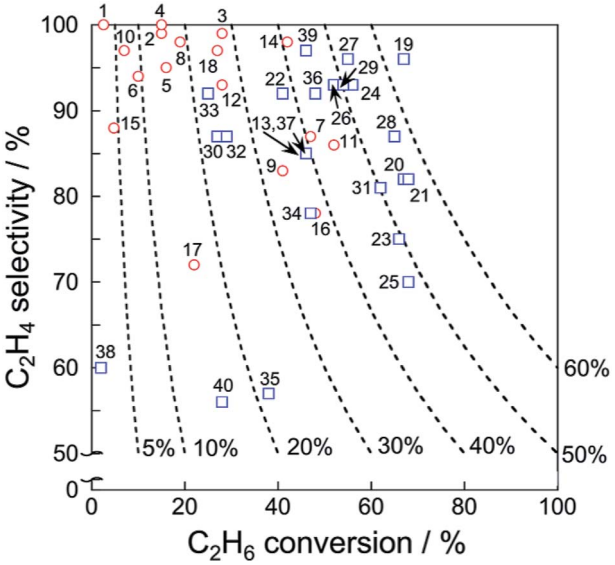

Fig. 11 Ethylene selectivity *vs.* ethane conversion of each catalyst presented in Tables 1 and 2. Dashed lines represent ethylene yield. Also, EDH in the absence and presence of CO_2 are shown respectively with red circles and blue squares.

using proton conducting materials such as barium zirconate ($BaZrO_3$) and barium cerate ($BaCeO_3$). Alternatively, supplying CO_2 to cathode results in CO formation.

Ding *et al.* performed electrochemical EDH at 673–773 K using $BaCeO_3$-based proton conducting materials as the anode.[180] They reported that electrochemical EDH proceeds without coke formation at 673 K. Increasing the reaction temperature induced coke formation and low ethylene selectivity. To mitigate coke formation, Zhang *et al.* used Ni and Cu doped niobium-based complexed oxides (proton conducting material) as the anode.[181] Ni–Cu alloys formed through the reduction of the anode contribute to the suppression of coke formation even at 973 K. Ethane conversion and ethylene selectivity are 66.3 and 99.7% respectively at 0.8 V. In combination with CO_2 reduction in the cathode, ethane conversion increased up to 75.2%. By contrast, Song *et al.* performed electrochemical EDH with CO_2 reduction using oxygen anion conducting materials.[182] They reported that γ-Al_2O_3 addition to lanthanum-based complexed oxide enhanced ethane conversion and ethylene selectivity without coke formation.

Researches on electrochemical EDH are focused on the performance and electric properties of anode materials. However, elucidation of activity–conductivity relationship is necessary for further improvement of the performance.

3.5.2. Photocatalytic EDH. Photocatalysis is a light-driven chemical reaction proceeding on semiconductors such as metal oxides, metal sulfides, and metal nitrides.[183] As shown in Fig. 12(b), photocatalysis is initiated by exciting electrons from the valence band (VB) to the conduction band (CB) through photon absorption. The photon energy must be greater than the band gap energy to excite the valence electrons. With the photoexcitation, holes are created in the VB. The photoexcited carriers (electrons and holes) migrate to the surface on which the redox reaction proceeds. The electron–hole pairs are easy to be recombined and, therefore, separation of the carriers from the bulk to the surface leads to a high photocatalytic activity. Metallic cocatalysts such as Pt and Pd are usually loaded on the semiconductors to promote the charge separation, namely inhibition of the recombination. Additional details of photocatalysis are reviewed in a literature.[183]

Photocatalytic EDH is performed by Zhang *et al.* using Pd/TiO_2 catalysts in combination with CO_2 reduction (Fig. 12(b)).[184] Pd/TiO_2 exhibited ethane conversion of 0.14% at 308 K and 0.2 MPa. The obtained conversion is corresponded to the equilibrium conversion at 498 K. It is explained that the forward and backward reactions require different energy and reaction

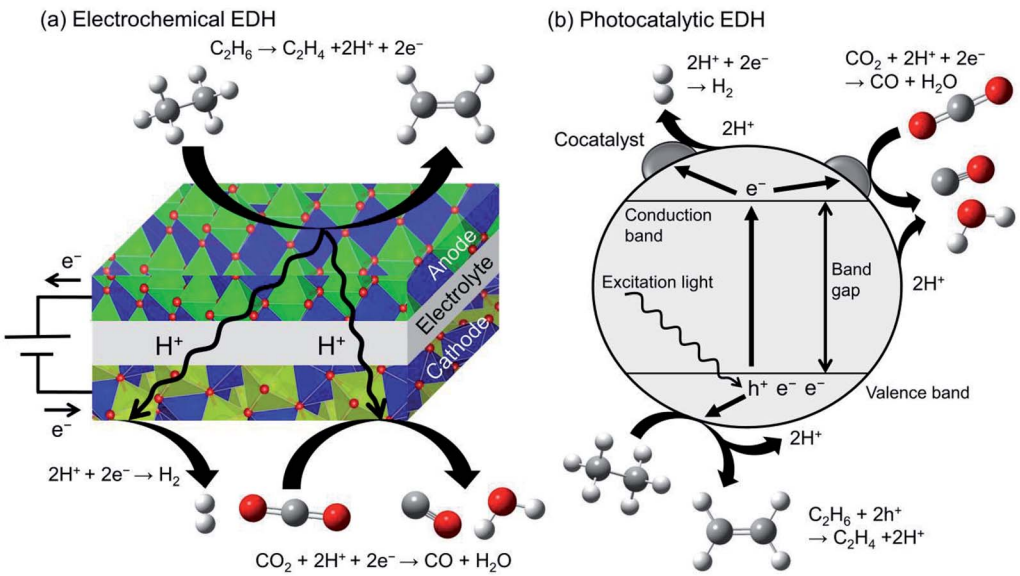

Fig. 12 Schematic images of (a) electrochemical EDH by a solid oxide electrolysis cell and (b) photocatalytic EDH over a particulate semiconductor with a cocatalyst.

mechanisms (irreversible).[185] They also conducted spin-trapping ESR and demonstrated clearly that the hydroxyl radicals (·OH) are formed on TiO_2 surface through oxidation of hydroxy groups with the holes. In addition to the holes, the hydroxyl radicals contribute to ethylene formation.

Producing chemicals from ethane through photocatalytic reactions are still immature research field. Practically using photocatalysts, the photocatalytic reactions must be visible light-driven. In addition to researches on materials science for controlling band gap energy, understanding the reaction mechanism is essential to design photocatalysts exhibiting high ethylene selectivity.

4. Dehydroaromatization of ethane

Ethane dehydroaromatization, denoted as EDA, forms BTX in one step.

$$3C_2H_6(g) \rightarrow C_6H_6(g) + 6H_2(g),\ \Delta_r H^\theta\ (298\ K) = 337\ kJ\ mol^{-1} \quad (14)$$

This reaction is an endothermic reaction similar to EDH. Therefore, high reaction temperatures at around 873 K are favorable to achieve high equilibrium conversion. From a practical perspective, the products are readily handled in terms of separation, storage and transportation because the gaseous reactant is converted to liquid products, potentially leading to a feasible process. However, commercial processes have not been developed yet using the natural gas resources (methane and ethane) in contrast with aromatization of C_3 and C_4 hydrocarbons.[120] This lack of development is attributable to high reaction temperatures, resulting in the rapid deactivation of zeolite-supported metal catalysts through coke formation.[186–189] Effective zeolite topology and active metals are briefly explained at the beginning of this chapter. Next, details of the nature of Zn/H-ZSM-5, the reaction pathways and deactivation by coke formation are described. Finally, aspects of the catalytic performance of the representative EDA catalysts are summarized.

4.1. Zeolite-supported metal catalysts

4.1.1. Effective zeolite topology for BTX formation. For EDA, the H-ZSM-5 zeolite modified with active metals is known to be an effective catalyst. In fact, MFI-type zeolite has three-dimensional micropore channel systems, which consist of straight and sinusoidal channels.[190,191] They comprise 10-membered rings with *ca.* 0.55 nm diameter, which closely approximates the kinetic diameters of BTX. Because of the micropore channels, the MFI-type zeolite exhibits shape selectivity to BTX formation. In addition, H-ZSM-5 has strong Brønsted acid sites (BAS), which catalyze various reactions such as isomerization, cracking, alkylation and hydrogen transfer based on the carbenium and carbonium ion chemistry. Details of the reactions over zeolite catalysts are described in the literature.[192]

The MEL-type zeolite (ZSM-11) is another candidate for the support.[193,194] Actually, ZSM-11 has similar micropore channel systems to those of ZSM-5, which consist of two straight channels.[190,191] However, the superiority of ZSM-11 compared to ZSM-5 has not been demonstrated clearly. The MWW-type zeolite presented by MCM-22 has not been used in contrast with methane dehydroaromatization.[195] Reportedly, MCM-22 has two independent micropore channel systems.[190,191] One comprises 12-membered ring cages connected to 10-membered ring windows. The other is a two-dimensional micropore channel system. Difference between methane and ethane dehydroaromatization are attributable to the kinds of active metals. Zn or Ga catalysts are used mainly for EDA in contrast with Mo catalysts for methane dehydroaromatization. The use of Mo might be promising for BTX formation in the case of MCM-22 support because of the different reaction pathways, as described in Section 4.2.

4.1.2. Active metals for EDA. The H-ZSM-5 zeolite is usually modified with active metals to facilitate ethane activation. Activating ethane at BAS is difficult because the formation of primary carbenium ions is unfavorable, resulting in low ethane conversion over H-ZSM-5 without the metal modification. In Section 4.2, the roles of the active metals are discussed in relation to the reaction pathway. As reported earlier, active metals including Pt, Ga, and Zn are effective for ethane activation.[196–200] However, Pt is expensive; it induces hydrogenolysis of ethane to methane under H_2 atmospheres.[35]

$$C_2H_6(g) + H_2(g) \rightarrow 2CH_4(g),\ \Delta_r H^\theta\ (298\ K) = -64.9\ kJ\ mol^{-1} \quad (15)$$

Also, H-ZSM-5-supported Mo and rhenium (Re) catalysts exhibit high performance for EDA[201–203] in addition to dehydroaromatization of methane.[204,205] However, these two metals are unsuitable for practical use because of sublimation of MoO_3 and rhenium oxide (Re_2O_7),[206,207] which probably exist in the pristine and regenerated catalysts, resulting in irreversible deactivation of the catalysts.

4.1.3. Structure and properties of zinc species on H-ZSM-5. Based on the reasons explained above, Ga or Zn modified H-ZSM-5 is mainly used for EDA. Detailed characteristics of the Ga species are described in Subsection 3.2.1. Here, the nature of Zn species on H-ZSM-5 is presented in detail. The nature of Zn species on H-ZSM-5 has been investigated by many research groups because of its wide applications to various chemical reactions such as methane conversion and alkylation of benzene.[208]

Preparation of Zn/H-ZSM-5 can be done using various methods such as impregnation, ion-exchange, physical mixing, and CVD.[209–212] The active Zn species on H-ZSM-5 are classifiable into two types: ZnO species and ion-exchanged Zn species. The first, ZnO, exists on the external and internal surfaces denoted respectively as macrocrystalline ZnO and ZnO clusters. These ZnO species are analyzed conveniently using UV-Vis spectroscopy.[209,212] Macrocrystalline ZnO exhibits an absorption band at *ca.* 370 nm attributed to its band gap energy. By contrast, ZnO clusters exhibit an absorption band at around 270 nm. Chen *et al.* reported that ZnO clusters were identified using laser-induced luminescence spectroscopy.[213] When excited by

a 244 nm laser, Zn/H-ZSM-5 containing ZnO clusters showed a purple luminescence band at *ca.* 440 nm. However, the ZnO species are reduced under reductive conditions at elevated temperatures. Some are exchanged with BAS (solid state ion-exchange), resulting in the formation of ion-exchanged Zn species and H_2O.[214]

$$ZnO + 2H^+–O_z \rightarrow O_z–Zn^{2+}–O_z + H_2O \quad (16)$$

Here, O_z represents the oxygen in the zeolite framework. This phenomenon was also observed in the case in which Zn metal was used instead of ZnO. Others are reduced to Zn metal vapor, resulting in the loss of Zn.

The existence of the ion-exchanged Zn species is roughly verified by temperature-programmed desorption of NH_3 (NH_3-TPD). In the TPD profile, two ammonia desorption peaks are observed respectively in low-temperature and high-temperature regions, denoted respectively as l-peak and h-peak.[215] The l-peak is attributed to the desorption of ammonia bonded to the ammonia adsorbed onto acid sites. The h-peak is ascribed to desorption of ammonia adsorbed onto the acid sites, which indicates that the peak area of l-peak does not reflect the amount of acid sites. Additionally, the desorbed ammonia derived from BAS is indistinguishable from that from Lewis acid sites.[216] Although the h-peak contains ammonia desorbed from BAS and Lewis acid sites, the h-peak intensity decreases after the ion-exchange,[209] indicating the exchange of BAS with Zn cations. The decrease in BAS can be verified using ^{1}H MAS NMR spectroscopy or NH_3-TPD with IR and mass spectrometry.[212,216] Formation of the ion-exchanged Zn species is verified by evaluating the electronic state of Zn because of its difference from that of ZnO.[210] XPS studies revealed that the ion-exchanged Zn species show a peak at *ca.* 1024 eV in the Zn $2p_{3/2}$ XP spectrum. In contrast, a peak corresponding to ZnO is observed at *ca*. 1021 eV.

Structures of the ion-exchanged Zn species are controversial. Berndt *et al.* proposed the structure of the ion-exchanged Zn.[211] They used temperature-programmed surface reaction (TPSR) with CO and observed formation of CO_2 and H_2, indicating the existence of $[Zn(OH)]^+$, as shown in Scheme 5. During TPSR with CO, the water gas shift reaction proceeds at $[Zn(OH)]^+$ and the nearest BAS, resulting in formation of the isolated Zn^{2+} (O_z–Zn^{2+}–O_z).

In addition, Biscardi *et al.* analyzed Zn/H-ZSM-5 using *in situ* Zn K-edge XANES spectroscopy.[217] The measurements were conducted in the presence of helium, hydrogen or propylene at up to 773 K. They concluded that $[Zn(OH)]^+$ in pristine Zn/H-ZSM-5 is dehydrated at the nearest BAS, resulting in the isolated Zn^{2+} interacting with two ion-exchange sites under the propane dehydrogenation atmosphere. In their study, Zn/H-ZSM-5 with a small loading amount of Zn (<1.3 wt%) was used and, therefore, they described that two Zn^{2+} cations bridged by an oxygen atom (O_z–Zn^{2+}–O–Zn^{2+}–O_z), denoted as binuclear Zn species, could be formed at high Zn loading amount. Almutairi *et al.* investigated the structures of Zn in H-ZSM-5 prepared by CVD, impregnation, and ion-exchange methods.[212] The isolated Zn species are formed by CVD. In contrast, the impregnation or ion-exchange method induces formation of Zn species of various kinds, including the isolated Zn and oxygenated Zn clusters. The specific structure of the oxygenated Zn clusters was not elucidated. According to Penzien *et al.*,[218] the structure of Zn in *BEA-type zeolite depends on the Zn loading amount. Concentration of the binuclear Zn species increases at Zn/Al $\geq$ 0.15. Therefore, the large amount of Zn would result in formation of the binuclear Zn species in the case of H-ZSM-5. Furthermore, Tamiyakul *et al.* reported that the ion-exchanged Zn species existing in pristine Zn/H-ZSM-5 was reduced under H_2 atmospheres based on XPS.[210] They proposed formation of ZnH^+ in the presence of H_2. Indeed, Zn hydrides were observed at room temperature using DRIFT spectroscopy.[219] Formation of ZnH^+ would be attributed to the promotive H_2 desorption at Zn sites through hydrogen back-spillover.[220–222] In contrast, Gao *et al.* also evaluated the electronic state of Zn by XPS after reduction with H_2 at various temperatures.[223] They described that ZnO clusters are reduced to $[Zn(OH)]^+$ at 573 K, and reported that conversion of $[Zn(OH)]^+$ to Zn^{2+} occurs at 673 K.

As described above, Zn species existing in H-ZSM-5 are diverse: ZnO, $[Zn(OH)]^+$, O_z–Zn^{2+}–O_z, O_z–Zn^{2+}–O–Zn^{2+}–O_z, and ZnH^+. Under EDA conditions, ZnO and $[Zn(OH)]^+$ are converted respectively to metallic Zn and O_z–Zn^{2+}–O_z. The former is vaporized, resulting in the loss of Zn. The latter is anticipated as a major candidate for the active sites. Aleksandrov and Vayssilov investigated EDH at the isolated Zn^{2+}, $[Zn(OH)]^+$ and ZnH^+ sites based on DFT.[224] The isolated Zn^{2+} at a paired Al site is more active for ethane activation than ZnH^+ at one Al site because of the vicinity of two Al centers. The existence of the binuclear Zn species has not been demonstrated clearly. Pidko and van Santen calculated energy diagrams of EDH at binuclear Zn sites using DFT calculations.[225] The binuclear Zn species is not favorable for EDH, which is the initial reaction of EDA, because

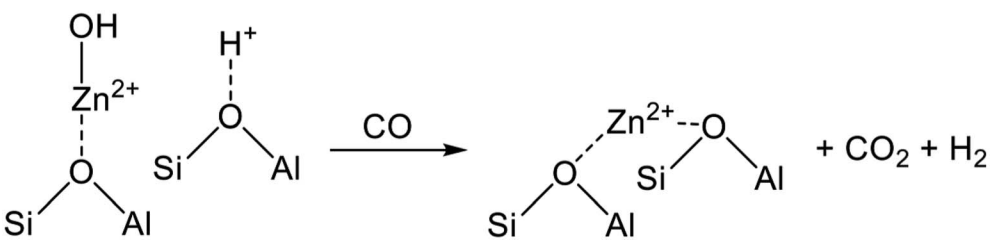

Scheme 5 Structural change from $[Zn(OH)]^+$ to isolated Zn^{2+} after the water gas shift reaction.

a stable intermediate is formed on the binuclear sites. However, the binuclear Zn species are presumed to be the active sites for EDA in recent studies.[226,227] Therefore, further studies to elucidate the structures of the Zn active sites must be conducted to clarify the nature of the structure–activity relation.

4.2. Reaction pathway of BTX formation

Reaction pathways of BTX formation were investigated using Pt, Zn, Ga, and Re/H-ZSM-5.[196,228–230] Because EDA is a complex reaction, the elucidation of each elementary step is challenging. Irrespective of the kind of active metal involved, the proposed reaction pathway is almost identical. As presented in Scheme 6, ethane is first dehydrogenated to ethylene at metal sites on the external or internal surface. Subsequently, ethylene is oligomerized, cyclized, and dehydrogenated to BTX in micropore channel systems. Under low conversion levels (low residence time), ethylene is the main product. However, selectivity to BTX and methane increases with decreased selectivity to ethylene under high conversion levels (high residence time). Also, C_3 and C_4 hydrocarbons, which are composed mainly of olefins, form during the reaction.

Hagen *et al.* demonstrated the formation of linear C_4 olefins using a recirculation reactor.[231] They proposed that the linear C_4 olefins are intermediates for BTX. Reportedly, oligomerization of ethylene proceeds even at room temperature.[232,233] In addition, ethylene is converted to propylene through oligomerization and cracking catalyzed by BAS.[234,235] Therefore, ethylene would first be oligomerized to C_4 olefins and would subsequently be cracked to propylene. Propylene could also be converted to BTX through a similar pathway of ethylene aromatization.[236,237] In contrast with Scheme 6, a recent study of aromatization of ethylene proposed that hydrocarbon species also contribute to the reaction, similarly to the methanol conversion to aromatic hydrocarbons.[238] It can be demonstrated based on ^{13}C MAS NMR that aliphatic sp^3 carbon species attributable to alkylated aromatic hydrocarbons formed through $^{13}C_2H_4$ aromatization are consumed after $^{12}C_2H_4$ aromatization.

Actually, the distribution of BTX depends on the reaction temperature.[196] At lower temperatures (<723 K), their proportion is in the order of xylenes > toluene > benzene. In a middle temperature range (773–823 K), the proportion of toluene increases. Furthermore, benzene formation increases at higher temperatures. This tendency is the case in aromatization of ethylene, propylene, and methanol.[236,239,240] Iglesia *et al.* performed dehydroaromatization of propane using ^{13}C-propane ($^{12}CH_3$–$^{13}CH_2$–$^{12}CH_3$).[241] They revealed that the number of ^{13}C atoms included in benzene and toluene are statistically distributed, indicating that the propane carbon chain is rearranged randomly during the reaction. This is true probably because interconversion among olefins, which are the intermediates for aromatic hydrocarbons, occurs quite rapidly. Haag *et al.* reported that an approximate equilibrium distribution was attained for propylene conversion to olefins at 723 and 823 K.[240] Depending on the reaction temperatures, light olefins are produced at higher temperatures, resulting in formation of light aromatic hydrocarbons such as benzene and toluene. Based on these results, Keipert *et al.* proposed that an olefin pool in which mutual olefins are equilibrated is formed during EDA.[229] Recently, Liang *et al.* reported the finding of BTX formed from different olefin intermediates based on transient kinetic studies of ethane and ethylene aromatization.[242] They proposed that the distribution of BTX might depend on the partial pressure of the olefin intermediates. In addition, Choudhary *et al.* reported that the proportion of BTX in aromatization of olefins is dependent on the space velocity.[237,243] Dependence of the proportion of BTX on space velocity (conversion) is similar to dependence on temperature. The partial pressure of the intermediates varies with conversion of reactants, which can be controlled by the space velocity and reaction temperature because aromatization reactions are sequential reactions. Inclusively, the distribution of BTX can be controlled in the case in which the interconversion of olefins occurs under kinetic conditions. Under such conditions, other possible reactions such as hydro-dealkylation and *trans*-alkylation of aromatic hydrocarbons, which are catalyzed by BAS, might also affect the distribution of BTX. Fundamentally, these reactions are not considered for EDA. In addition to elucidation of the reaction pathway, the side reactions described above should be regarded as maximizing selectivity to valuable chemicals such as *p*-xylene.

The nature of active metals is a crucially important factor in the aromatization of light alkanes. Generally, the first dehydrogenation step (C–H bond activation) is a rate-determining step over H-ZSM-5. The active metals promote dehydrogenation of the alkanes. In contrast, Biscardi and Iglesia proposed the hydrogen desorption step as rate-determining in dehydrogenation of propane over Zn/H-ZSM-5.[220] Indeed, Zn/H-ZSM-5 and ZnO exhibit hydrogen spillover and back-spillover effects,[221,222] indicating that hydrogen desorption is promoted by virtue of Zn. In addition, the active metals influence BTX formation. Over H-

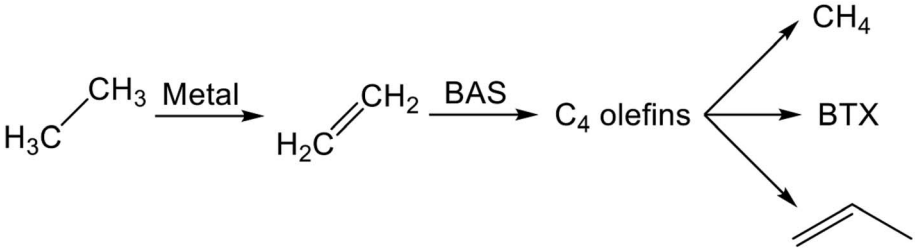

Scheme 6 Reaction pathway of EDA.

ZSM-5, dienes and cyclodienes are intermediates in aromatization of ethylene, as reported by Batchu *et al.*[244] As presented in Scheme 7, aromatization over H-ZSM-5 fundamentally proceeds through oligomerization, cyclization, and dehydrogenation *via* hydrogen transfer with formation of alkanes.[245] In contrast, modification of H-ZSM-5 with Zn, Ga and silver (Ag) enhances selectivity to BTX in aromatization of ethylene,[223,226,238,246–248] indicating the promotive effect of the active metals on formation of aromatic hydrocarbons. Bandiera and Taârit proposed that dehydrogenation of cycloalkenes to form BTX competes with ethane activation.[249] They demonstrated that EDA was inhibited by addition of cyclohexadiene, regarded as a precursor of BTX, to the ethane feed.[250] Therefore, the active metals contribute not only activation of light alkanes but the formation of BTX because aromatization of the intermediates would readily proceed in comparison to hydrogen transfer catalyzed by BAS. A recent study of methanol to aromatic hydrocarbons also revealed that introduction of Zn to H-ZSM-5 enhances dehydrogenation ability, which leads to high yield of aromatic hydrocarbons, and which inhibits hydrogen transfer because of the small amount of BAS induced by ion-exchange with Zn.[251]

Recent studies of Mo/H-ZSM-5 for dehydroaromatization of methane have elicited new insights into the formation of aromatics.[252–255] Generally, Mo/H-ZSM-5 is presumed to be a bifunctional catalyst, as reviewed in the literature.[256–258] Briefly, activation of methane proceeds on carburized Mo species; subsequently, BAS promote aromatization of intermediates. Kosinov *et al.* demonstrated that methane conversion to benzene proceeds over Mo/Silicalite-1 with no Brønsted acidity.[252] They proposed that BAS contribute to high dispersion of Mo species, which efficiently convert methane to benzene. Their studies further revealed the existence of radical carbon species in micropores.[253] These confined carbon species play a role as intermediates in the dehydroaromatization of methane.[254] Therefore, in analogous to methane, EDA over Mo/H-ZSM-5 is expected to proceed through the radical carbon species, as depicted in Scheme 8. Indeed, Uslamin *et al.* demonstrated clearly in EDA that reduction of Mo and subsequent building up the carbon species in micropores proceed through ethane decomposition.[259] Benzene formation is initiated after the two-step induction period. Such was not observed in case of Ga/H-ZSM-5.

In addition, Gascon and co-workers explored the nature of the carbon included in Mo (oxy-)carbide.[260] They performed ^{12}CO treatment to form Mo (oxy-)carbide and conducted pulse experiments using $^{13}CH_4$. They demonstrated that ^{12}C included in Mo (oxy-)carbide is consumed to form ethylene and benzene. The nature of Mo species is also investigated elsewhere.[261–263] It is noteworthy that the characteristic nature of Mo (oxy-)carbide might not be exhibited in the aromatization of ethylene. After dehydroaromatization of methane and ethylene over Mo/H-ZSM-5, stable selectivity to aromatic hydrocarbons and reactive carbonaceous deposits was achieved in the case of methane.[264] They concluded that ethylene is unlikely to be the main intermediate for dehydroaromatization of methane. Therefore, the reaction pathway of BTX formation would be considered carefully in EDA over Mo/H-ZSM-5.

4.3. Catalyst deactivation by coke formation

Deactivation of H-ZSM-5 modified with active metals presents great difficulty. Coke formation over H-ZSM-5 is catalyzed by BAS through over-oligomerization and aromatization. In addition, elements of the active metals and their amounts influence the ethylene to aromatic hydrocarbons step.[238] Various techniques including thermogravimetric analysis, and Raman and ^{13}C MAS NMR spectroscopy have been used to analyze coke species. Aspects of coke formation on zeolite catalysts are summarized in the literature.[265] The coke species are mainly polycyclic aromatic

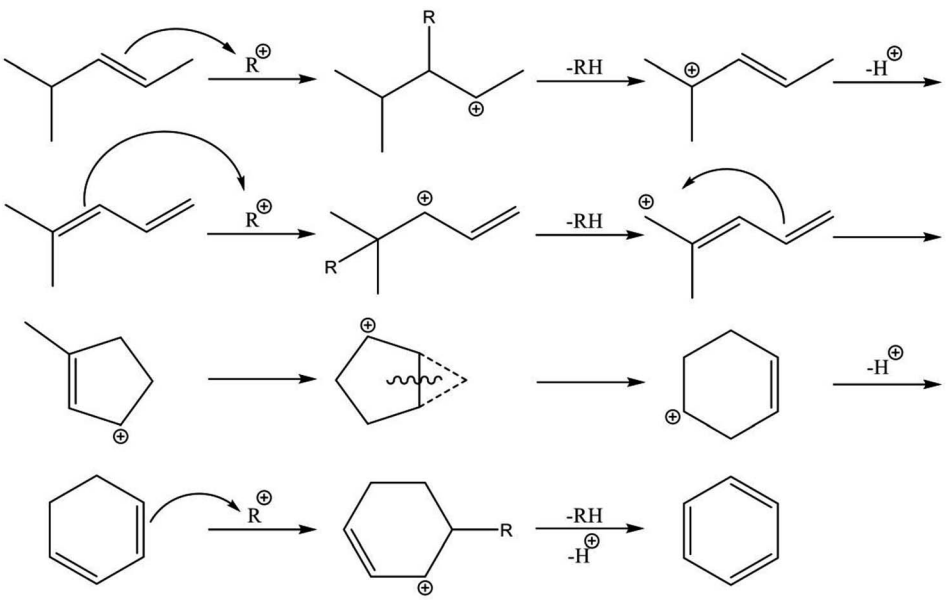

Scheme 7 Aromatization of oligomers over H-ZSM-5.

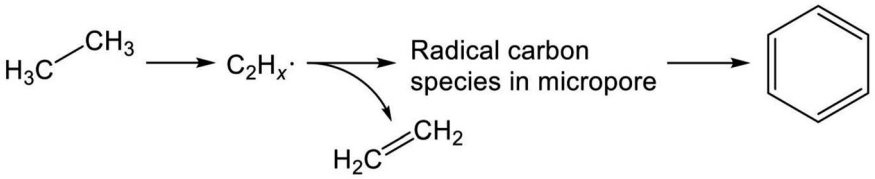

Scheme 8 Possible reaction pathway of EDA over Mo/H-ZSM-5.

hydrocarbons under aromatization conditions. They induce blocking of micropore channels, leading to eventual deactivation of the catalysts. Therefore, the catalysts must be periodically regenerated under oxidative conditions.[266]

Addition of a promoter to a metal-modified H-ZSM-5 is one effective means of suppressing coke formation. Robinson *et al.* performed Fe addition to Mo/ZSM-5 for EDA.[266] The Fe promoter improved the catalytic stability because carbon nanotubes were formed on the H-ZSM-5 external surface. Formation of the carbon nanotubes, which have ordered structures, is expected to maintain openings of the micropore channels. Another example is Pt addition to Ga/H-ZSM-5.[267] In addition to the stability, Ga–Pt/H-ZSM-5 exhibited higher ethane conversion and selectivity to aromatic hydrocarbons than Ga/H-ZSM-5 and Pt/H-ZSM-5. The high stability of Ga–Pt/H-ZSM-5 would be attributed to consecutive removal of the coke species through hydrogenolysis during the reaction. Indeed, Marecot *et al.* performed TPSR with H_2 using coke-deposited Pt, Re and iridium (Ir) catalysts.[268] Methane formation through hydrogenolysis of the deposited coke was verified. The methane formation temperature increased in the order of Ir < Re < Pt.

Modification of BAS is an alternative means of inhibiting coke formation. The BAS are located on the external and internal surfaces. However, the BAS on the external surface are not expected to exhibit shape selectivity to BTX formation because they are not located in the micropore channels. The formation of coke precursors such as polycyclic aromatic hydrocarbons is rather favorable. Epelde *et al.* investigated the deactivation pathways of H-ZSM-5 during ethylene conversion to propylene.[269] They inferred that the coke species composed of condensed aromatics and long aliphatic chains are deposited on the external surface, which indicates that the removal of BAS located at the external surface is effective. Inagaki *et al.* reported that nitric acid (HNO_3) treatment of H-ZSM-5 synthesized without organic structure-directing agent removes Al (BAS) selectively from its external surface.[270] In addition, control of the distribution of framework Al would also be an effective means. Generally, the MFI topology has 12 T-sites, which are candidates for Al sites, as shown in Fig. 13. Among them, T1, T4, and T6 do not face the intersections. Although T4 is located at the sinusoidal channels, T1 and T6 are located at the straight channels. The distribution of the Al sites can be controlled by the synthesis conditions.[271,272] Liu *et al.* synthesized H-ZSM-5 with different Al distribution and performed ethane and ethylene aromatization over Pt/H-ZSM-5.[273] They concluded that BAS located at the intersections tend to contribute to the formation of aromatic hydrocarbons. H-ZSM-5 with much Al located at the intersections exhibited high and stable conversion and BTX yield. The remaining Al sites located at the straight and sinusoidal channels can be expected to induce coke formation, resulting in the blocking of micropore channels and the inhibition of diffusion of the products.

The proximity of a Brønsted acid site to the nearest one is regarded as important for the suppression of coke formation. Zhang *et al.* prepared Zn/H-ZSM-5 using nano-ZSM-5 with crystalline size of approximately 100 nm.[227] Because of the suppression of carbon deposition, Zn/nano-ZSM-5 exhibits higher stability for EDA than Zn/micro-ZSM-5 does. In micropores of nano-ZSM-5, the short diffusion path can be expected to facilitate the escape of aromatic hydrocarbons, leading to mitigation of consecutive conversion of the products to coke. It is noteworthy that nano-ZSM-5 has a larger external surface area than micro-ZSM-5. Assuming that the density of BAS on the external surface is equal to that on the internal surface, the contribution of BAS located on the external surface would be enhanced in the case of nano-ZSM-5. Therefore, selectivity to products would also depend on the crystalline size because BAS on the external surface do not exhibit shape selectivity to BTX formation. Introduction of mesopores, which probably improve mass diffusion, to ZSM-5 enhances the catalytic performance.[274] It also contributes to an increase in coke capacity; ZSM-5 with the mesopores exhibited high activity and stability in spite of the large amount of carbon deposition.[275] In another study, Ye *et al.* synthesized pillared ZSM-5 with various lamellar thickness.[276] They performed EDA over Mo/pillared-ZSM-5 and demonstrated that ZSM-5 with thick layers (long diffusion path) and moderate Si/Al ratios exhibited high activity, selectivity to

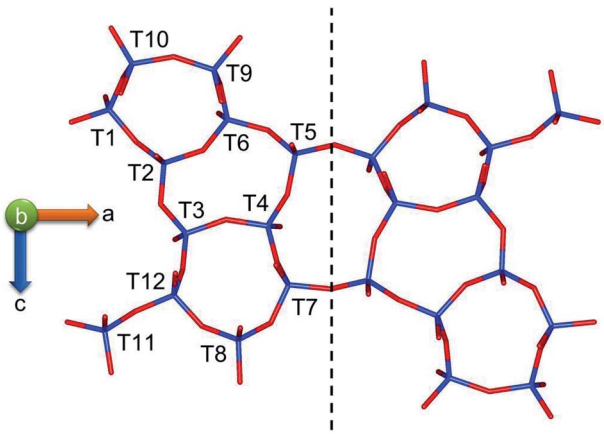

Fig. 13 Twelve T-sites of MFI topology.

Table 3 Representative performance of EDA catalysts

Catalyst	Si/Al	Temperature/K	C_2H_6 conversion/%	Aromatics selectivity/%	Aromatics yield/%	Ref.
Ga/H-ZSM-5	15	873	28.2	57.3	16.2	199
Pt–Ga/H-ZSM-5	21	823	34.4	62.0	22.1	278
Zn–H-ZSM-5	11.5	773	15.4	48.0	7.4	226
Zn–H-ZSM-5	15	873	41.9	48.0	20.1	242
Mo/ZSM-11	27	973	99.7	56.7	56.5	193
Re/ZSM-5	30	873	48.0	59.0	28.2	203

aromatic hydrocarbons, and stability. In their study, ZSM-5 with low Si/Al ratios (the large amount of BAS) is unfavorable because of its rapid deactivation. However, ZSM-5 with low Si/Al ratios has high ion-exchange capacity, which is rather convenient to incorporate large amounts of ion-exchanged metal cations such as Zn. In this case, dealumination as a post-synthetic method is a useful means to control the amount of BAS. Saito *et al.* performed steam treatment of Zn/H-ZSM-5 for EDA.[277] They revealed that the framework Al with proton (BAS) is preferentially dealuminated through the steam treatment after ion-exchange with Zn. However, the framework Al with Zn cations was unaffected by the steam treatment. The steam-treated Zn/H-ZSM-5 exhibited high and stable activity for EDA, respectively, by virtue of optimal and large amounts of BAS and Zn.

4.4. Performance of EDA catalysts

Representative performance of EDA catalysts is presented in Table 3. The reaction is conducted at around 873 K using zeolites with low Si/Al ratios. Further studies of the properties of active metals and reaction mechanism are indispensable to enhance their catalytic performance. In addition, the improvement of catalytic stability is crucially important for the practical use of EDA on a large scale. As described above, studies of various kinds have been conducted, examining promoters, zeolite synthesis, and post-synthetic methods to elucidate methods of inhibiting coke formation. From a practical perspective, the reaction system would be pressurized to make the reactor volume small because large amounts of hydrogen are formed through EDA (reaction (14)). Recent study of dehydroaromatization of methane[255] has revealed that catalytic stability can be improved at 15 bar through the rapid hydrogenation of coke at high pressure. Additionally, hydrogen removal from the reaction system can enhance BTX yield.[278] Therefore, further studies conducted from chemical engineering perspectives must be undertaken to support EDA process development.

5. Conclusion and perspectives

Recent progress in catalysts for EDH and EDA has been described from the perspective of the nature of active sites and reaction mechanisms. In terms of EDH, supported Pt-, Cr- and Ga-based catalysts have been intensively investigated.

Generally speaking, Pt-based catalysts exhibit high activity and selectivity at low temperatures (<873 K). Fundamentally, promoters such as Sn are used for Pt catalysts to enhance their performance. Modification of Pt with Sn decreases the number of "cus-Pt", at which sites hydrogenolysis and coke formation proceed, if Pt–Sn alloys are formed or not. In addition, the promoters affect the electronic state of Pt, although the intrinsic effects are under discussion (electron donation or modification of the Pt 5d bands). The change in the electronic state of Pt enhances TOF concomitantly with fast desorption of ethylene. For Pt-based catalysts, structure–activity and electronic state–activity relations can be expected to be mutually interactive. Practically, the structure of Pt active sites (fcc or hcp) must be examined with the surface composition of Pt/promoter ratios. Determination of the active sites contributes to construction of calculation models. In theoretical studies, coverage of adsorbates such as hydrogen affects the stability of the intermediates. Therefore, calculation conditions must be close to the realistic ones to predict the active site characteristics.

By contrast to Pt catalysts, Cr-based catalysts are cost-effective. Among the Cr species, trivalent monochromate and polychromate are candidates for use as active sites in the absence of CO_2. On the other hand, CO_2 co-feed enhances activity by virtue of redox properties. For the Cr catalysts, it is challenging to evaluate the activities of respective Cr species because both monochromate and polychromate usually exist. In addition, the reaction mechanisms that take place in the presence of CO_2 must be evaluated carefully: for instance, kinetic analyses at low conversion levels and elucidation of CO_2 roles using isotopes must be supported. Additional studies are expected to be indispensable for the assessment of Cr catalysts. However, these findings reveal that ethane activation is rather more favorable through the redox mechanism than through the Langmuir–Hinshelwood-like mechanism. Such is the case with other metal oxides with redox properties, such as La–Mn perovskites. These redox materials can be applied to EDH using chemical looping.[279]

Because of their cost-effectiveness and non-toxicity compared to Pt and Cr, Ga-based catalysts are also candidates for use for EDH. However, additional improvement of the catalytic performance must be done to make the Ga-based catalysts alternative candidates for them. It is noteworthy that zeolite supports in addition to the conventional supports including Al_2O_3, SiO_2 and TiO_2 are used for Ga in contrast with Pt and Cr. Zeolite supports contribute to the formation of characteristic Ga active sites, as described in Subsection 3.3.1. The Ga species in zeolite micropores have various structures such as $[GaH_2]^+$ and GaO clusters dependent on the reaction atmospheres. In recent studies, zeolite-supported Fe and In catalysts are applied to EDH. The characteristic nature of zeolite can increase the feasible options of active metals.

As for EDA catalysts, Ga, Zn or Mo supported on ZSM-5 has been investigated. Studies of EDA have specifically pursued elucidation of the structure of ion-exchanged Zn in ZSM-5 and methods to inhibit coke formation. Among the proposed structures, the isolated Zn (O_z–Zn^{2+}–O_z) is a probable active site. The specific structures of oxygenated Zn species such as the binuclear Zn (O_z–Zn^{2+}–O–Zn^{2+}–O_z) are not demonstrated clearly. However, it is plausible that the properties of Zn depend on, for example, the preparation method and loading amount. To suppress coke formation, the Al location and the proximity of BAS in ZSM-5 should be controlled. For Mo, the reaction pathway is expected to be different from that of Zn. Therefore, further studies of the reaction pathways of BTX formation are expected to be indispensable for improvement of the catalytic performance.

To implement EDA practically, the activity and selectivity to aromatic hydrocarbons must be enhanced. Considering studies of EDH, CO_2 co-feed is one option. Indeed, EDA with CO_2 was performed over Ga and Zn/H-ZSM-5.[280,281] Furthermore, other active metals with redox properties are expected to exhibit high catalytic performance for EDA with CO_2 because the ethane activation step can proceed *via* the redox mechanism (Scheme 1). In the presence of CO_2, Ga/H-ZSM-5 is apparently preferable to Zn/H-ZSM-5, probably because H_2O is formed through RWGS. The existence of H_2O promotes dehydrogenation in case of Ga/H-ZSM-5.[135] The isolated Zn can be converted to $[Zn(OH)]^+$, which would be inactive for aromatization, in the presence of H_2O. In addition, a recent study of dehydroaromatization of methane has demonstrated that addition of metallic Zr to Mo/H-ZSM-5 enhances catalytic performance by virtue of efficient removal of H_2 through hydrogen absorption with $ZrH_{1.75}$ formation.[282] Removal of H_2 from the reaction system can shift the equilibrium of EDH forward, leading to high catalytic activity.

In conclusion, fundamental research efforts must be undertaken to develop catalytic processes for converting ethane to valuable chemicals. Recent progress in catalytic science and technology for ethane conversion has gradually revealed the intrinsic characteristics of the active sites indispensable to ethane activation. These new findings are expected to develop not only methods for efficient production of the valuable chemicals from ethane but for bridging technologies to guide future petrochemical industry development to production of a sustainable society.

Notes

The molecules and crystalline structures were visualized by GaussView 5 and VESTA softwares.[283,284]

Conflicts of interest

There are no conflicts to declare.

Acknowledgements

H. S. acknowledges financial support from JSPS KAKENHI (Grant-in-Aid for JSPS Fellows) Grant number 19J10015. Y. S. acknowledges support by JST-CREST (grant no. JPMJCR1423).

References

1 J. Boulamanti and A. Moya, *Renewable Sustainable Energy Rev.*, 2017, **68**, 1205.
2 *Forecast of Global Supply and Demand Trends for Petrochemical Products (from 2010 to 2023)*, METI Japan, https://www.meti.go.jp/english/press/2019/1017_001.html, 2019, accessed on 20/5/2020.
3 J. J. H. B. Sattler, J. Ruiz-Martinez, E. Santillan-Jimenez and B. M. Weckhuysen, *Chem. Rev.*, 2014, **114**, 10613.
4 P. Tian, Y. Wei, M. Ye and Z. Liu, *ACS Catal.*, 2015, **5**, 1922.
5 U. Olsbye, S. Svelle, K. P. Lillerud, Z. H. Wei, Y. Y. Chen, J. F. Li, J. G. Wang and W. B. Fan, *Chem. Soc. Rev.*, 2015, **44**, 7155.
6 N. Popoff, E. Mazoyer, J. Pelletier, R. M. Gauvin and M. Taoufik, *Chem. Soc. Rev.*, 2013, **42**, 9035.
7 R. Grabowski, *Catal. Rev.: Sci. Eng.*, 2006, **48**, 199.
8 C. A. Gärtner, A. C. van Veen and J. A. Lercher, *ChemCatChem*, 2013, **5**, 3196.
9 F. O. Rice and K. F. Herzfeld, *J. Am. Chem. Soc.*, 1934, **56**, 284.
10 M. L. Poutsma, *J. Anal. Appl. Pyrolysis*, 2000, **54**, 5.
11 M. W. M. van Goethem, S. Barendregt, J. Grievink, J. A. Moulijn and P. J. T. Verheijen, *Ind. Eng. Chem. Res.*, 2007, **46**, 4045.
12 C. Batiot and B. K. Hodnett, *Appl. Catal., A*, 1996, **137**, 179.
13 K. M. Sundaram and G. F. Froment, *Ind. Eng. Chem. Fundam.*, 1978, **17**, 174.
14 K. M. Van Geem, G. J. Heynderichx and G. B. Marin, *AIChE J.*, 2004, **50**, 173.
15 E. Heracleous and A. A. Lemonidou, *Appl. Catal., A*, 2004, **269**, 123.
16 G. F. Froment, B. O. van de Steene, P. S. van Damme, S. Narayanan and A. G. Goossens, *Ind. Eng. Chem. Process Des. Dev.*, 1976, **15**, 495.
17 K. M. Sundaram, P. S. van Damme and G. F. Froment, *AIChE J.*, 1981, **27**, 946.
18 S. Mahamulkar, K. Yin, P. K. Agrawal, R. J. Davis, C. W. Jones, A. Malek and H. Shibata, *Ind. Eng. Chem. Res.*, 2016, **55**, 9760.
19 S. H. Symoens, N. Olahova, A. E. M. Gandarillas, H. Karimi, M. R. Djokic, M. Reyniers, G. B. Marin and K. M. Van Geem, *Ind. Eng. Chem. Res.*, 2018, **57**, 16117.
20 A. E. M. Gandarillas, K. M. Van Geem, M. Reyniers and G. B. Marin, *Ind. Eng. Chem. Res.*, 2014, **53**, 6358.
21 S. A. Sarris, N. Olahova, K. Verbeken, M. Reyniers, G. B. Marin and K. M. Van Geem, *Ind. Eng. Chem. Res.*, 2017, **56**, 1424.
22 S. Wauters and G. B. Marin, *Ind. Eng. Chem. Res.*, 2002, **41**, 2379.
23 M. Takahashi, Y. Enjo and S. Uramaru, *US Pat.*, US0318593A1, 2011.
24 S. S. A. Petrone, R. L. Deuis, F. Kong, and Y. Chen, *US Pat.*, US9421526B2, 2016.
25 S. Wang, W. Peng, Q. Fu, Z. Deng, Z. Wu, C. Lin, Y. Gu, X. Zhang, and L. B. Kool, *US Pat.*, US10138431B2, 2018.

26 M. M. Bhasin, J. H. McCain, B. V. Vora, T. Imai and P. R. Pujadó, *Appl. Catal., A*, 2001, **221**, 397.
27 P. R. Cottrell and M. E. Fettis, *US Pat.*, US5087792, 1992.
28 J. H. Kwak, J. Hu, D. Mei, C.-W. Yi, D. H. Kim, C. H. F. Peden, L. F. Allard and J. Szanyi, *Science*, 2009, **325**, 1670.
29 L. Shi, G.-M. Deng, W.-C. Li, S. Miao, Q.-N. Wang, W.-P. Zhang and A.-H. Lu, *Angew. Chem., Int. Ed.*, 2015, **54**, 13994.
30 F. Cavani, F. Trifirò and A. Vaccari, *Catal. Today*, 1991, **11**, 173.
31 J. Feng, Y. He, Y. Liu, Y. Du and D. Li, *Chem. Soc. Rev.*, 2015, **44**, 5291.
32 K. Takehira, *Appl. Clay Sci.*, 2017, **136**, 112.
33 D. Akporiaye, S. F. Jensen, U. Olsbye, F. Rohr, E. Rytter, M. Rønnekleiv and A. I. Spjelkavik, *Ind. Eng. Chem. Res.*, 2001, **40**, 4741.
34 R. M. Rioux, H. Song, J. D. Hoefelmeyer, P. Yang and G. A. Somorjai, *J. Phys. Chem. B*, 2005, **109**, 2192.
35 H. Song, R. M. Rioux, J. D. Hoefelmeyer, R. Komor, K. Niesz, M. Grass, P. Yang and G. A. Somorjai, *J. Am. Chem. Soc.*, 2006, **128**, 3027.
36 Z. Peng, F. Somodi, S. Helveg, C. Kisielowski, P. Specht and A. T. Bell, *J. Catal.*, 2012, **286**, 22.
37 G. Peng, D. Gerceker, M. Kumbhalkar, J. A. Dumesic and M. Mavrikakis, *Catal. Sci. Technol.*, 2018, **8**, 2159.
38 J. Wu, Z. Peng and A. T. Bell, *J. Catal.*, 2014, **311**, 161.
39 J. Zhu, M.-L. Yang, Y. Yu, Y.-A. Zhu, Z.-J. Sui, X.-G. Zhou, A. Holmen and D. Chen, *ACS Catal.*, 2015, **5**, 6310.
40 V. Galvita, G. Siddiqi, P. Sun and A. T. Bell, *J. Catal.*, 2010, **271**, 209.
41 S. Saerens, M. K. Sabbe, V. V. Galvita, E. A. Redekop, M.-F. Reyniers and G. B. Marin, *ACS Catal.*, 2017, **7**, 7495.
42 A. Hook, J. D. Massa and F. E. Celik, *J. Phys. Chem. C*, 2016, **120**, 27307.
43 M. H. Hansen, J. K. Nørskov and T. Bligaaed, *J. Catal.*, 2019, **374**, 161.
44 H.-A. Ha, E. T. Baxter, A. C. Cass, S. A. Anderson and A. N. Alexandrova, *J. Am. Chem. Soc.*, 2017, **139**, 11568.
45 Z. Han, S. Li, F. Jiang, T. Wang, X. Ma and J. Gong, *Nanoscale*, 2014, **6**, 10000.
46 P. Sun, G. Siddiqi, M. Chi and A. T. Bell, *J. Catal.*, 2010, **274**, 192.
47 G. Siddiqi, P. Sun, V. Galvita and A. T. Bell, *J. Catal.*, 2010, **274**, 200.
48 E. A. Redekop, V. V. Galvita, H. Poelman, V. Bliznuk, C. Detavernier and G. B. Marin, *ACS Catal.*, 2014, **4**, 1812.
49 M. Filez, E. A. Redekop, H. Poelman, V. V. Galvita, R. K. Ramachandran, J. Dendooven, C. Detavernier and G. B. Marin, *Chem. Mater.*, 2014, **26**, 5936.
50 Z. Yu, J. A. Sawada, W. An and S. M. Kuznichi, *AIChE J.*, 2015, **61**, 4367.
51 V. J. Cybulskis, B. C. Bukowski, H.-T. Tseng, J. R. Gallagher, Z. Wu, E. Wegener, A. J. Kropf, B. Ravel, F. H. Ribeiro, J. Greeley and J. T. Miller, *ACS Catal.*, 2017, **7**, 4173.
52 P. Sun, G. Siddiqi, W. C. Vining, M. Chi and A. T. Bell, *J. Catal.*, 2011, **282**, 165.
53 E. C. Wegener, Z. Wu, H.-T. Tseng, J. R. Gallagher, Y. Ren, R. E. Diaz, F. H. Ribeiro and J. T. Miller, *Catal. Today*, 2018, **299**, 146.
54 S. Fang, K. Zhnag, C. Wang, L. Ma, Q. Zhang, Q. Liu, L. Chen, Q. Zhang and Z. Tian, *RSC Adv.*, 2017, **7**, 22836.
55 Q. Zhang, K. Zhang, S. Zhang, Q. Liu, L. Chen, X. Li, C. Wang and L. Ma, *J. Catal.*, 2018, **368**, 79.
56 A. Virnovskaia, S. Jørgensen, J. Hafizovic, Ø. Prytz, E. Kleimenov, M. Hävecher, H. Bluhm, A. Knop-Gericke, R. Schlögl and U. Olsbye, *Surf. Sci.*, 2007, **601**, 30.
57 A. Virnovskaia, S. Morandi, E. Rytter, G. Ghiotti and U. Olsbye, *J. Phys. Chem. C*, 2007, **111**, 14732.
58 A. Virnovskaia, E. Rytter and U. Olsbye, *Ind. Eng. Chem. Res.*, 2008, **47**, 7176.
59 E. Jimenez-Izal, H. Zhai, J.-Y. Liu and A. N. Alexandrova, *ACS Catal.*, 2018, **8**, 8346.
60 E. Jimenez-Izal, J.-Y. Liu and A. N. Alexandrova, *J. Catal.*, 2019, **374**, 93.
61 W. Yu, M. D. Porosoff and J. G. Chen, *Chem. Rev.*, 2012, **112**, 5780.
62 S. Furukawa and T. Komatsu, *ACS Catal.*, 2017, **7**, 735.
63 A. Hook and F. E. Celik, *J. Phys. Chem. C*, 2017, **121**, 17882.
64 L. Deng, H. Miura, T. Shishido, Z. Wang, S. Hosokawa, K. Teramura and T. Tanaka, *J. Catal.*, 2018, **365**, 277.
65 L. Deng, T. Shishido, K. Teramura and T. Tanaka, *Catal. Today*, 2014, **232**, 33.
66 L. Deng, H. Miura, T. Shishido, S. Hosokawa, K. Teramura and T. Tanaka, *ChemCatChem*, 2014, **6**, 2680.
67 L. Deng, H. Miura, T. Ohkubo, T. Shishido, Z. Wang, S. Hosokawa, K. Teramura and T. Tanaka, *Catal. Sci. Technol.*, 2019, **9**, 947.
68 A. Moscu, Y. Schuurman, L. Veyre, C. Thieuleux and F. Meunier, *Chem. Commun.*, 2014, **50**, 8590.
69 C. Dupont, D. Loffreda, F. Delbecq and Y. Jugnet, *J. Phys. Chem. C*, 2007, **111**, 8524.
70 Q. Wang, D. Tichit, F. Meunier and H. Guesmi, *J. Phys. Chem. C*, 2020, **124**, 9979.
71 A. Moscu, C. Theodoridi, L. Cardenas, C. Thieuleux, D. Motta-Meria, G. Agostini, Y. Schuurman and F. Meunier, *J. Catal.*, 2018, **359**, 76.
72 T. Avanesian, S. Dai, M. J. Kale, G. W. Graham, X. Pan and P. Christopher, *J. Am. Chem. Soc.*, 2017, **139**, 4551.
73 M. S. Kumar, D. Chen, A. Holmen and J. C. Walmsley, *Catal. Today*, 2009, **142**, 17.
74 H. N. Pham, J. J. H. B. Sattler, B. M. Weckhuysen and A. K. Datye, *ACS Catal.*, 2016, **6**, 2257.
75 A. Iglesias-Juez, A. M. Beale, K. Maaijen, T. C. Weng, P. Glatzel and B. M. Weckhuysen, *J. Catal.*, 2010, **276**, 268.
76 Y. Uemura, Y. Inada, K. K. Bando, T. Sasaki, N. Kamiuchi, K. Eguchi, A. Yagishita, M. Nomura, M. Tada and Y. Iwasawa, *Phys. Chem. Chem. Phys.*, 2011, **13**, 15833.
77 H. Xin, N. Schweitzer, E. Nikolla and S. Linic, *J. Chem. Phys.*, 2010, **132**, 111101.
78 D. Bazin, D. Sayers, J. J. Rehr and C. Mottet, *J. Phys. Chem. B*, 1997, **101**, 5332.

79 J. T. Miller, A. J. Kropf, Y. Zha, J. R. Regalbuto, L. Delannoy, C. Louis, E. Bus and J. A. van Bokhoven, *J. Catal.*, 2006, **240**, 222.
80 M. W. Tew, J. T. Miller and J. A. van Bokhoven, *J. Phys. Chem. C*, 2009, **113**, 15140.
81 D. Tibiletti, A. Goguet, D. Reid, F. C. Meunier and R. Burch, *Catal. Today*, 2006, **113**, 94.
82 H. Xin, A. Holewinski, N. Schweitzer, E. Nikolla and S. Linic, *Top. Catal.*, 2012, **55**, 376.
83 E. C. Wegener, B. C. Bukowski, D. Yang, Z. Wu, A. J. Kropf, W. N. Delgass, J. Greeley, G. Zhang and J. T. Miller, *ChemCatChem*, 2020, **12**, 1325.
84 R. G. Windham and B. E. Koel, *J. Phys. Chem.*, 1990, **94**, 1489.
85 L. Liwu, Z. Tao, Z. Jingling and X. Zhusheng, *Appl. Catal.*, 1990, **67**, 11.
86 H. Lieske, A. Sárkány and J. Völter, *Appl. Catal.*, 1987, **30**, 69.
87 Catofin® Propane/Butane Dehydrogenation, McDermott, https://www.mcdermott.com/What-We-Do/Technology/Lummus/Petrochemicals/Olefins/Propylene-Production/Propane-Butane-Dehydrogenation, 2018, accessed on 18/5/2020.
88 U. Olsbye, A. Virnovskaia, Ø. Prytz, S. J. Tinnemans and B. M. Weckhuysen, *Catal. Lett.*, 2005, **103**, 143.
89 F. Cavani, M. Koutyrev, F. Trifirò, A. Bartolini, D. Ghisletti, R. Iezzi, A. Santucci and G. Del Piero, *J. Catal.*, 1996, **158**, 236.
90 B. M. Weckhuysen and R. A. Schoonheydt, *Catal. Today*, 1999, **51**, 223.
91 R. L. Puurunen and B. M. Weckhuysen, *J. Catal.*, 2002, **210**, 418.
92 S. D. Yim and I.-S. Nam, *J. Catal.*, 2004, **221**, 601.
93 Y. Wang, Y. Ohishi, T. Shishido, Q. Zhang, W. Yang, Q. Guo, H. Wan and K. Takehira, *J. Catal.*, 2003, **220**, 347.
94 K. Takehira, Y. Ohishi, T. Shishido, T. Kawabata, K. Takaki, Q. Zhang and Y. Wang, *J. Catal.*, 2004, **224**, 404.
95 V. Z. Fridman, R. Xing and M. Severance, *Appl. Catal., A*, 2016, **523**, 39.
96 M. Botavina, C. Barzan, A. Piovano, L. Braglia, G. Agostini, G. Martra and E. Groppo, *Catal. Sci. Technol.*, 2017, **7**, 1690.
97 D. He, Y. Zhang, S. Yang, Y. Mei and Y. Luo, *ChemCatChem*, 2018, **10**, 5434.
98 N. Mimura, M. Okamoto, H. Yamashita, S. T. Oyama and K. Murata, *J. Phys. Chem. B*, 2006, **110**, 21764.
99 X. Shi, S. Ji, K. Wang and C. Li, *Energy Fuels*, 2008, **22**, 3631.
100 T. V. M. Rao, E. M. Zahidi and A. Sayari, *J. Mol. Catal. A: Chem.*, 2009, **301**, 159.
101 H. H. Shin and S. McIntosh, *ACS Catal.*, 2015, **5**, 95.
102 D. Shee and A. Sayari, *Appl. Catal., A*, 2010, **389**, 155.
103 S. Wang, K. Murata, T. Hayakawa, S. Hamakawa and K. Suzuki, *Catal. Lett.*, 1999, **63**, 59.
104 L. Liu, H. Li and Y. Zhang, *Catal. Today*, 2006, **115**, 235.
105 Y. Cheng, L. Zhou, J. Xu, C. Miao, W. Hua, Y. Yue and Z. Gao, *Microporous Mesoporous Mater.*, 2016, **234**, 370.
106 Y. Cheng, C. Miao, W. Hua, Y. Yue and Z. Gao, *Appl. Catal., A*, 2017, **532**, 111.
107 S. Wang and Z. H. Zhu, *Energy Fuels*, 2004, **18**, 1126.
108 S. Wang, K. Murata, T. Hayakawa, S. Hamakawa and K. Suzuki, *Appl. Catal., A*, 2000, **196**, 1.
109 N. Mimura, I. Takahara, M. Inaba, M. Okamoto and K. Murata, *Catal. Commun.*, 2002, **3**, 257.
110 T. A. Bugrova, V. V. Dutov, V. A. Svetlichnyi, V. C. Corberán and G. V. Mamontov, *Catal. Today*, 2019, **333**, 71.
111 J. Baek, H. J. Yun, D. Yun, Y. Choi and J. Yi, *ACS Catal.*, 2012, **2**, 1893.
112 T. Shishido, K. Shimamura, K. Teramura and T. Tanaka, *Catal. Today*, 2012, **185**, 151.
113 A. S. Al-Awadi, A. M. El-Toni, S. M. Al-Zahrani, A. E. Abasaeed, M. Alhoshan, A. Khan, J. P. Labis and A. Al-Fatesh, *Appl. Catal., A*, 2019, **584**, 117114.
114 X. Shi, S. Ji and K. Wang, *Catal. Lett.*, 2008, **125**, 331.
115 F. Rahmani, M. Haghighi and B. Mohammadkhanai, *Microporous Mesoporous Mater.*, 2017, **242**, 34.
116 S. Deng, H. Li, S. Li and Y. Zhang, *J. Mol. Catal. A: Chem.*, 2007, **268**, 169.
117 X. Li, S. Liu, H. Chen, S. Luo, F. Jing and W. Chu, *ACS Omega*, 2019, **4**, 22562.
118 K. Nakagawa, M. Okamura, N. Ikenaga, T. Suzuki and T. Kobayashi, *Chem. Commun.*, 1998, 1025.
119 A. Bhan and W. N. Delgass, *Catal. Rev.: Sci. Eng.*, 2008, **50**, 19.
120 G. Giannetto, R. Monque and R. Galiasso, *Catal. Rev.: Sci. Eng.*, 1994, **36**, 271.
121 K. M. Dooley, T. F. Guidry and G. L. Price, *J. Catal.*, 1995, **157**, 66.
122 A. Ausavasukhi and T. Sooknoi, *Catal. Commun.*, 2014, **45**, 63.
123 N. Rane, A. R. Overweg, V. B. Kasansky, R. A. van Santen and E. J. M. Hensen, *J. Catal.*, 2006, **239**, 478.
124 V. B. Kazansky, I. R. Subbotina, R. A. van Santen and E. J. M. Hensen, *J. Catal.*, 2004, **227**, 263.
125 V. B. Kazansky, I. R. Subbotina, R. A. van Santen and E. J. M. Hensen, *J. Catal.*, 2005, **233**, 351.
126 A. B. Getsoian, U. Das, J. Camocho-Bunquin, G. Zhang, J. R. Gallagher, B. Hu, S. Cheah, J. A. Schaidle, D. A. Ruddy, J. E. Hensley, T. R. Krause, L. A. Curtiss, J. T. Miller and A. S. Hock, *Catal. Sci. Technol.*, 2016, **6**, 6339.
127 M. W. Schreiber, C. P. Plaisance, M. Baumgärtl, K. Reuter, A. Jentys, R. Bermejo-Deval and J. A. Lercher, *J. Am. Chem. Soc.*, 2018, **140**, 4849.
128 M. S. Pereira and M. A. C. Nascimento, *J. Phys. Chem. B*, 2006, **110**, 3231.
129 M. S. Pereira, A. M. da Silva and M. A. C. Nascimento, *J. Phys. Chem. C*, 2011, **115**, 10104.
130 E. A. Pidko, V. B. Kazansky, E. J. M. Hensen and R. A. van Santen, *J. Catal.*, 2006, **240**, 73.
131 E. A. Pidko, E. J. M. Hensen and R. A. van Santen, *J. Phys. Chem. C*, 2007, **111**, 13068.
132 Y. V. Joshi and K. T. Thomson, *J. Catal.*, 2007, **246**, 249.
133 E. Mansoor, M. Head-Gordon and A. T. Bell, *ACS Catal.*, 2018, **8**, 6146.
134 V. B. Kazansky, I. R. Subbotina, N. Rane, R. A. van Santen and E. J. M. Hensen, *Phys. Chem. Chem. Phys.*, 2005, **7**, 3088.

135 E. J. M. Hensen, E. A. Pidko, N. Rane and R. A. van Santen, *Angew. Chem., Int. Ed.*, 2007, **46**, 7273.
136 E. A. Pidko, E. J. M. Hensen, G. M. Zhidomirov and R. A. van Santen, *J. Catal.*, 2008, **255**, 139.
137 E. A. Pidko, R. A. van Santen and E. J. M. Hensen, *Phys. Chem. Chem. Phys.*, 2009, **11**, 2893.
138 E. A. Pidko and R. A. van Santen, *J. Phys. Chem. C*, 2009, **113**, 4246.
139 K. Nakagawa, C. Kajita, Y. Ide, M. Okamura, S. Kato, H. Kasuya, N. Ikenaga, T. Kobayashi and T. Suzuki, *Catal. Lett.*, 2000, **64**, 215.
140 M. Zinkevich and F. Aldinger, *J. Am. Ceram. Soc.*, 2004, **87**, 683.
141 B. Zheng, W. Hua, Y. Yue and Z. Gao, *J. Catal.*, 2005, **232**, 143.
142 H. Seki, H. Saito, K. Toko, Y. Hosono, T. Higo, J. G. Seo, S. Maeda, K. Hashimoto, S. Ogo and Y. Sekine, *Appl. Catal., A*, 2019, **581**, 23.
143 K. Nishi, K. Shimizu, M. Takamatsu, H. Yoshida, A. Satsuma, T. Tanaka, S. Yoshida and T. Hattori, *J. Phys. Chem. B*, 1998, **102**, 10190.
144 K. Shimizu, M. Takamatsu, K. Nishi, H. Yoshida, A. Satsuma, T. Tanaka, S. Yoshida and T. Hattori, *J. Phys. Chem. B*, 1999, **103**, 1542.
145 S. E. Collins, M. A. Baltanás, J. L. G. Fierro and A. L. Bonivardi, *J. Catal.*, 2002, **211**, 252.
146 S. E. Collins, M. A. Baltanás and A. L. Bonivardi, *Langmuir*, 2005, **21**, 962.
147 W. Jochum, S. Penner, K. Föttinger, R. Kramer, G. Rupprechter and B. Klötzer, *J. Catal.*, 2008, **256**, 268.
148 Y. Pan, D. Mei, C. Liu and Q. Ge, *J. Phys. Chem. C*, 2011, **115**, 10140.
149 V. B. Kazansky, I. R. Subbotina, A. A. Pronin, R. Schlögl and F. C. Jentoft, *J. Phys. Chem. B*, 2006, **110**, 7975.
150 A. A. Gabrienko, S. S. Arzumanov, A. V. Toktarev and A. G. Stepanov, *Chem. Phys. Lett.*, 2010, **496**, 148.
151 Y. Cheng, T. Lei, C. Miao, W. Hua, Y. Yue and Z. Gao, *Microporous Mesoporous Mater.*, 2018, **268**, 235.
152 H. Xiao, J. Zhang, P. Wang, X. Wang, F. Pang, Z. Zhang and Y. Tan, *Catal. Sci. Technol.*, 2016, **6**, 5183.
153 K. Nakagawa, C. Kajita, K. Okumura, N. Ikenaga, M. Nishitani-Gamo, T. Ando, T. Kobayashi and T. Suzuki, *J. Catal.*, 2001, **203**, 87.
154 T. Lei, Y. Cheng, C. Miao, W. Hua, Y. Yue and Z. Gao, *Fuel Process. Technol.*, 2018, **177**, 246.
155 R. Koirala, R. Buechel, F. Krumeich, S. E. Pratsinis and A. Baiker, *ACS Catal.*, 2015, **5**, 690.
156 Z. Shen, J. Liu, H. Xu, Y. Yue, W. Hua and W. Shen, *Appl. Catal., A*, 2009, **356**, 148.
157 X. Zhang, Q. Ye, B. Xu and D. He, *Catal. Lett.*, 2007, **117**, 140.
158 R. Koirala, R. Buechel, S. E. Pratsinis and A. Baiker, *Appl. Catal., A*, 2016, **527**, 96.
159 R. Koirala, O. V. Safonova, S. E. Pratsinis and A. Baiker, *Appl. Catal., A*, 2018, **552**, 77.
160 F. Solymosi and R. Németh, *Catal. Lett.*, 1999, **62**, 197.
161 M. D. Porosoff, M. N. Z. Myint, S. Kattel, Z. Xie, E. Gomez, P. Liu and J. G. Chen, *Angew. Chem., Int. Ed.*, 2015, **54**, 15501.
162 S. Yao, B. Yan, Z. Jiang, Z. Liu, Q. Wu, J. H. Lee and J. G. Chen, *ACS Catal.*, 2018, **8**, 5374.
163 Z. Ji, H. Lv, X. Pan and X. Bao, *J. Catal.*, 2018, **361**, 94.
164 X. Yang, T. Wei, B. Chi, J. Pu and J. Li, *J. Catal.*, 2019, **377**, 629.
165 H. Saito, H. Seki, Y. Hosono, T. Higo, J. G. Seo, S. Maeda, K. Hashimoto, S. Ogo and Y. Sekine, *J. Phys. Chem. C*, 2019, **123**, 26272.
166 K. Toko, K. Ito, H. Saito, Y. Hosono, K. Murakami, S. Misaki, T. Higo, S. Ogo, H. Tsuneki, S. Maeda, K. Hashimoto, H. Nakai and Y. Sekine, *J. Phys. Chem. C*, 2020, **124**, 10462.
167 B. Yan, S. Yao and J. G. Chen, *ChemCatChem*, 2020, **12**, 494.
168 Z. Wu, E. C. Wegener, H.-T. Tseng, J. R. Gallagher, J. W. Harris, R. E. Diaz, Y. Ren, F. H. Ribeiro and J. T. Miller, *Catal. Sci. Technol.*, 2016, **6**, 6965.
169 Q. Xie, T. Lei, C. Miao, W. Hua, Y. Yue and Z. Gao, *Catal. Lett.*, 2020, **150**, 2013.
170 Y. He, Y. Song, D. A. Cullen and S. Laursen, *J. Am. Chem. Soc.*, 2018, **140**, 14010.
171 Y. He, Y. Song and S. Laursen, *ACS Catal.*, 2019, **9**, 10464.
172 L.-C. Wang, Y. Zhang, J. Xu, W. Diao, S. Karakalos, B. Liu, X. Song, W. Wu, T. He and D. Ding, *Appl. Catal., B*, 2019, **256**, 117816.
173 Z. Maeno, S. Yasumura, X. Wu, M. Huang, C. Liu, T. Toyano and K. Shimizu, *J. Am. Chem. Soc.*, 2020, **142**, 4820.
174 K. Nakagawa, C. Kajita, N. Ikenaga, T. Suzuki, T. Kobayashi, M. Nishitani-Gamo and T. Ando, *J. Phys. Chem. B*, 2003, **107**, 4048.
175 X. Zhao and X. Wang, *Catal. Commun.*, 2006, **7**, 633.
176 M. H. Jeong, J. Sun, G. Y. Han, D. H. Lee and J. W. Bae, *Appl. Catal., B*, 2020, **270**, 118887.
177 T. Baidya, N. van Vegten and A. Baiker, *Top. Catal.*, 2011, **54**, 881.
178 T. V. Sagar, M. Surendar, D. Padmakar, G. Parameswaram, N. Lingaiah, K. S. R. Rao, I. A. K. Reddy, C. Sumana and P. S. S. Prasad, *Catal. Lett.*, 2017, **147**, 82.
179 K. D. Kreuer, *Annu. Rev. Mater. Res.*, 2003, **33**, 333.
180 D. Ding, Y. Zhang, W. Wu, D. Chen, M. Liu and T. He, *Energy Environ. Sci.*, 2018, **11**, 1710.
181 X. Zhang, L. Ye, H. Li, F. Chen and K. Xie, *ACS Catal.*, 2020, **10**, 3505.
182 Y. Song, L. Lin, W. Feng, X. Zhang, Q. Dong, X. Li, H. Lv, Q. Liu, F. Yang, Z. Liu, G. Wang and X. Bao, *Angew. Chem., Int. Ed.*, 2019, **58**, 16043.
183 Q. Wang and K. Domen, *Chem. Rev.*, 2020, **120**, 919.
184 R. Zhang, H. Wang, S. Tang, C. Liu, F. Dong, H. Yue and B. Liang, *ACS Catal.*, 2018, **8**, 9280.
185 L. Yuliati and H. Yoshida, *Chem. Soc. Rev.*, 2008, **37**, 1592.
186 Y. Ono, *Catal. Rev.: Sci. Eng.*, 1992, **34**, 179.
187 M. A. Bañares, *Catal. Today*, 1999, **51**, 319.
188 A. Hagen and F. Roessner, *Catal. Rev.: Sci. Eng.*, 2000, **42**, 403.

189 Y. Xiang, H. Wang, J. Cheng and J. Matsubu, *Catal. Sci. Technol.*, 2018, **8**, 1500.
190 C. Baerlocher, L. B. McCusker and D. H. Olson, *Atlas of Zeolite Framework Types*, Elsevier, Amsterdam, 6th edn, 2007.
191 *Database of Zeolite Structure, Structure Commission of the International Zeolite Association*, http://www.iza-structure.org/databases/, 2017, accessed on 14/4/2020.
192 M. Stöcker, *Microporous Mesoporous Mater.*, 2005, **82**, 257.
193 O. A. Anunziata, G. A. Eimer and L. B. Pierella, *Appl. Catal., A*, 1999, **182**, 267.
194 O. A. Anunziata, G. A. Eimer and L. B. Pierella, *Catal. Lett.*, 2001, **75**, 93.
195 Y. Shu, D. Ma, L. Xu, Y. Xu and X. Bao, *Catal. Lett.*, 2000, **70**, 67.
196 K.-H. Steinberg, U. Mroczek and F. Roessner, *Appl. Catal.*, 1990, **66**, 37.
197 A. Hagen, F. Roessner, I. Weingart and B. Spliethoff, *Zeolites*, 1995, **15**, 270.
198 V. I. Yakerson, T. V. Vasina, L. I. Lafer, V. P. Sytnyk, G. L. Dykh, A. V. Mokhov, O. V. Bragin and Kh. M. Minachev, *Catal. Lett.*, 1989, **3**, 339.
199 P. Schulz and M. Baerns, *Appl. Catal.*, 1991, **78**, 15.
200 F. Roessner, A. Hagen, U. Mroczek, H. G. Karge and K.-H. Steinberg, *Stud. Surf. Sci. Catal.*, 1993, **75**, 1707.
201 F. Solymosi and A. Szőke, *Appl. Catal., A*, 1998, **166**, 225.
202 A. Krogh, A. Hagen, T. W. Hansen, C. H. Christensen and I. Schmidt, *Catal. Commun.*, 2003, **4**, 627.
203 F. Solymosi and P. Tolmacsov, *Catal. Lett.*, 2004, **93**, 7.
204 L. Wang, L. Tao, M. Xie, G. Xu, J. Huang and Y. Xu, *Catal. Lett.*, 1993, **21**, 35.
205 L. Wang, R. Ohnishi and M. Ichikawa, *Catal. Lett.*, 1999, **62**, 29.
206 R. W. Borry III, Y. H. Kim, A. Huffsmith, J. A. Reimer and E. Iglesia, *J. Phys. Chem. B*, 1999, **103**, 5787.
207 C. Bolivar, H. Charcosset, R. Frety, M. Primet, L. Tournayan, C. Betizeau, G. Leclercq and R. Maurel, *J. Catal.*, 1975, **39**, 249.
208 G. Chen, Y. Zhao, L. Shang, G. I. N. Waterhouse, X. Kang, L.-Z. Wu, C.-H. Tung and T. Zhang, *Adv. Sci.*, 2016, **3**, 1500424.
209 X. Niu, J. Gao, Q. Miao, M. Dong, G. Wang, W. Fan, Z. Qin and J. Wang, *Microporous Mesoporous Mater.*, 2014, **197**, 252.
210 S. Tamiyakul, T. Sooknoi, L. L. Lobban and S. Jongpatiwut, *Appl. Catal., A*, 2016, **525**, 190.
211 H. Berndt, G. Lietz and J. Völter, *Appl. Catal., A*, 1996, **146**, 365.
212 S. M. T. Almutairi, B. Mezari, P. C. M. M. Magusin, E. A. Pidko and E. J. M. Hensen, *ACS Catal.*, 2012, **2**, 71.
213 J. Chen, Z. Feng, P. Ying and C. Li, *J. Phys. Chem. B*, 2004, **108**, 12669.
214 A. Hagen, E. Schneider, A. Kleinert and F. Roessner, *J. Catal.*, 2004, **222**, 227.
215 F. Lónyi and J. Valyon, *Microporous Mesoporous Mater.*, 2001, **47**, 239.
216 N. Katada, *Mol. Catal.*, 2018, **458**, 116.
217 J. A. Biscardi, G. D. Meitzner and E. Iglesia, *J. Catal.*, 1998, **179**, 192.
218 J. Penzien, A. Abraham, J. A. van Bokhoven, A. Jentys, T. E. Müller, C. Sievers and J. A. Lercher, *J. Phys. Chem. B*, 2004, **108**, 4116.
219 V. B. Kazansky and A. I. Serykh, *Phys. Chem. Chem. Phys.*, 2004, **6**, 3760.
220 J. A. Biscardi and E. Iglesia, *J. Catal.*, 1999, **182**, 117.
221 L. A. Dufresne and R. Le Van Mao, *Catal. Lett.*, 1994, **25**, 371.
222 S. Triwahyono, A. A. Jalil, R. R. Mukti, M. Musthofa, N. A. M. Razali and M. A. A. Aziz, *Appl. Catal., A*, 2011, **407**, 91.
223 J. Gao, C. Wei, M. Dong, G. Wang, Z. Li, Z. Qin, J. Wang and W. Fan, *ChemCatChem*, 2019, **11**, 3892.
224 H. A. Aleksandrov and G. N. Vayssilov, *Catal. Today*, 2010, **152**, 78.
225 E. A. Pidko and R. A. van Santen, *J. Phys. Chem. C*, 2007, **111**, 2643.
226 A. Mehdad and R. F. Lobo, *Catal. Sci. Technol.*, 2017, **7**, 3562.
227 Y. Zhang, S. Wu, X. Xu and H. Jiang, *Catal. Sci. Technol.*, 2020, **10**, 835.
228 A. Hagen, F. Roessner and W. Reschetilowski, *Chem. Eng. Technol.*, 1995, **18**, 414.
229 O. P. Keipert, D. Wolf, P. Schulz and M. Baerns, *Appl. Catal., A*, 1995, **131**, 347.
230 L. Ma and X. Zou, *Appl. Catal., B*, 2019, **243**, 703.
231 A. Hagen, O. P. Keipert and F. Roessner, *Stud. Surf. Sci. Catal.*, 1996, **101**, 781.
232 A. G. Stepanov, M. L. Luzgin, V. N. Romannikov, V. N. Sidelnikov and E. A. Paukshtis, *J. Catal.*, 1998, **178**, 466.
233 J. N. Kondo and K. Domen, *J. Mol. Catal. A: Chem.*, 2003, **199**, 27.
234 T. Koyama, Y. Hayashi, H. Horie, S. Kawauchi, A. Matsumoto, Y. Iwase, Y. Sakamoto, A. Miyaji, K. Motokura and T. Baba, *Phys. Chem. Chem. Phys.*, 2010, **12**, 2541.
235 Y. Iwase, Y. Sakamoto, A. Shiga, A. Miyaji, K. Motokura, T. Koyama and T. Baba, *J. Phys. Chem. C*, 2012, **116**, 5182.
236 M. Shibata, H. Kitagawa, Y. Sendoda and Y. Ono, *Stud. Surf. Sci. Catal.*, 1986, **28**, 717.
237 V. R. Choudhary, D. Panjala and S. Banerjee, *Appl. Catal., A*, 2002, **231**, 243.
238 E. A. Uslamin, H. Saito, N. Kosinov, E. Pidko, Y. Sekine and E. J. M. Hensen, *Catal. Sci. Technol.*, 2020, **10**, 2774.
239 V. R. Choudhary, S. Banerjee and D. Panjala, *Microporous Mesoporous Mater.*, 2002, **51**, 203.
240 W. O. Haag, R. M. Lago and P. G. Rodewald, *J. Mol. Catal.*, 1982, **17**, 161.
241 E. Iglesia, J. E. Baumgartner and G. L. Price, *J. Catal.*, 1992, **134**, 549.
242 T. Liang, H. Toghiani and Y. Xiang, *Ind. Eng. Chem. Res.*, 2018, **57**, 15301.
243 V. R. Choudhary, P. Devadas, S. Banerjee and A. K. Kinage, *Microporous Mesoporous Mater.*, 2001, **47**, 253.

244 R. Batchu, V. V. Galvita, K. Alexopoulos, K. Van der Borght, H. Poelman, M.-F. Reyniers and G. B. Marin, *Appl. Catal., A*, 2017, **538**, 207.
245 M. Guisnet, N. S. Gnep, D. Aittaleb and Y. J. Doyemet, *Appl. Catal., A*, 1992, **87**, 255.
246 P. Qiu, J. H. Lunsford and M. P. Rosynek, *Catal. Lett.*, 1998, **52**, 37.
247 H. Coqueblin, A. Richard, D. Uzio, L. Pinard, Y. Pouilloux and F. Epron, *Catal. Today*, 2017, **289**, 62.
248 M.-F. Hsieh, Y. Zhou, H. Thirumalai, L. C. Grabow and J. D. Rimer, *ChemCatChem*, 2017, **9**, 1675.
249 J. Bandiera and Y. B. Taârit, *Appl. Catal., A*, 1997, **152**, 43.
250 J. Bandiera and Y. B. Taarit, *Appl. Catal., A*, 1997, **161**, L43.
251 I. Pinilla-Herrero, E. Borfecchia, J. Holzinger, U. V. Mentzel, F. Joensen, K. A. Lomachenko, S. Bordiga, C. Lamberti, G. Berlier, U. Olsbye, S. Svelle, J. Skibsted and P. Beato, *J. Catal.*, 2018, **362**, 146.
252 N. Kosinov, F. J. A. G. Coumans, E. A. Uslamin, A. S. G. Wijplema, B. Mezari and E. J. M. Hensen, *ACS Catal.*, 2017, **7**, 520.
253 N. Kosinov, A. S. G. Wijpkema, E. Uslamin, R. Rohling, F. J. A. G. Coumans, B. Mezari, A. Parastaev, A. S. Poryvaev, M. V. Fedin, E. A. Pidko and E. J. M. Hensen, *Angew. Chem., Int. Ed.*, 2018, **57**, 1016.
254 N. Kosinov, E. A. Uslamin, F. J. A. G. Coumans, A. S. G. Wijpkema, R. Y. Rohling and E. J. M. Hensen, *ACS Catal.*, 2018, **8**, 8459.
255 N. Kosinov, E. A. Uslamin, L. Meng, A. Parastaev, Y. Liu and E. J. M. Hensen, *Angew. Chem., Int. Ed.*, 2019, **58**, 7068.
256 Z. R. Ismagilov, E. V. Matus and L. T. Tsikoza, *Energy Environ. Sci.*, 2008, **1**, 526.
257 J. J. Spivey and G. Hutchings, *Chem. Soc. Rev.*, 2014, **43**, 792.
258 I. Vollmer, I. Yarulina, F. Kapteijn and J. Gascon, *ChemCatChem*, 2019, **11**, 39.
259 E. A. Uslamin, H. Saito, Y. Sekine, E. J. M. Hensen and N. Kosinov, *Catal. Today*, DOI: 10.1016/j.cattod.2020.04.021, in press.
260 I. Vollmer, B. van der Linden, S. Ould-Chikh, A. Aguilar-Tapia, I. Yarulina, E. Abou-Hamad, Y. G. Sheider, A. I. O. Suarez, J.-L. Hazemann, F. Kapteijn and J. Gascon, *Chem. Sci.*, 2018, **9**, 4801.
261 I. Vollmer, N. Kosinov, Á. Szécsényi, G. Li, I. Yarulina, E. Abou-Hamad, A. Gurinov, S. Ould-Chikh, A. Aguilar-Tapia, J.-L. Hazemann, E. Pidko, E. Hensen, F. Kapteijn and J. Gascon, *J. Catal.*, 2019, **370**, 321.
262 I. Vollmer, S. Ould-Chikh, A. Aguilar-Tapia, G. Li, E. Pidko, J.-L. Hazemann, F. Kapteijn and J. Gascon, *J. Am. Chem. Soc.*, 2019, **141**, 18814.
263 G. Li, I. Vollmer, C. Liu, J. Gascon and E. A. Pidko, *ACS Catal.*, 2019, **9**, 8731.
264 I. Vollmer, E. Abou-Hamad, J. Gascon and F. Kapteijn, *ChemCatChem*, 2020, **12**, 544.
265 M. Guisnet, L. Costa and F. R. Ribeiro, *J. Mol. Catal. A: Chem.*, 2009, **305**, 69.
266 B. Robinson, X. Bai, A. Samanta, V. Abdelsayed, D. Shekhawat and J. Hu, *Energy Fuels*, 2018, **32**, 7810.
267 A. Samanta, X. Bai, B. Robinson, H. Chen and J. Hu, *Ind. Eng. Chem. Res.*, 2017, **56**, 11006.
268 P. Marecot, S. Peyrovi, D. Bahloul and J. Barbier, *Appl. Catal.*, 1990, **66**, 181.
269 E. Epelde, M. Ibañez, A. T. Aguayo, A. G. Gayubo, J. Bilbao and P. Castaño, *Microporous Mesoporous Mater.*, 2014, **195**, 284.
270 S. Inagaki, S. Shinoda, Y. Kaneko, K. Takeuchi, R. Komatsu, Y. Tsuboi, H. Yamazaki, J. N. Kondo and Y. Kubota, *ACS Catal.*, 2013, **3**, 74.
271 J. Dědeček, Z. Sobalík and B. Wichterlová, *Catal. Rev.: Sci. Eng.*, 2012, **54**, 135.
272 T. Yokoi, H. Mochizuki, S. Namba, J. N. Kondo and T. Tatsumi, *J. Phys. Chem. C*, 2015, **119**, 15303.
273 H. Liu, H. Wang, A.-H. Xing and J.-H. Cheng, *J. Phys. Chem. C*, 2019, **123**, 15637.
274 Y. Wang, A. Caiola, B. Robinson, Q. Li and J. Hu, *Energy Fuels*, 2020, **34**, 3100.
275 F. Goodarzi, R. P. Thumbayil, K. Enemark-Rasmussen, J. Mielby, T. T. M. Nguyen, P. Beato, F. Joensen and S. Kegnæs, *ChemCatChem*, 2020, **12**, 1519.
276 J. Ye, L. Bai, B. Liu, H. Tian, J. Hu, F. Polo-Garzon, R. T. Mayes, Z. Wu and Y. Fang, *Ind. Eng. Chem. Res.*, 2019, **58**, 7094.
277 H. Saito, S. Inagaki, K. Kojima, Q. Han, T. Yabe, S. Ogo, Y. Kubota and Y. Sekine, *Appl. Catal., A*, 2018, **549**, 76.
278 O. V. Chetina, T. V. Vasina and V. V. Lunin, *Appl. Catal., A*, 1995, **131**, 7.
279 X. Zhu, Q. Imtiaz, F. Donat, C. R. Müller and F. Li, *Energy Environ. Sci.*, 2020, **13**, 772.
280 E. Gomez, X. Nie, J. H. Lee, Z. Xie and J. G. Chen, *J. Am. Chem. Soc.*, 2019, **141**, 17771.
281 A. Mehdad, N. S. Gould, B. Xu and R. F. Lobo, *Catal. Sci. Technol.*, 2018, **8**, 358.
282 A. Kumar, K. Song, L. Liu, Y. Han and A. Bhan, *Angew. Chem., Int. Ed.*, 2018, **57**, 15577.
283 R. Dennington, T. A. Keith and J. M. Millam, *GaussView (Version 5)*, Semichem Inc., Shawnee Mission, KS, 2009.
284 K. Momma and F. Izumi, *J. Appl. Crystallogr.*, 2011, **44**, 1272.